Voltage-driven polymer translocation through entropic traps and nanopores

Petr Hotmar*, Ravi Chella†
Department of Chemical and Biomedical Engineering,
Florida State University

Abstract

We analyze the transport and separation of biomolecules (polyelectrolytes and DNA in particular) under electrokinetic flows in microscale geometries of critical dimensions on the order of the characteristic size of the molecules, i.e. radius of gyration for chains. The governing systems of field equations are discretized by finite differences on boundary-fitted overlapping grids, while the polymer is coarse-grained into a bead-spring model that follows Langevin dynamics. The objective of the work is a mesoscale-level treatment of hydrodynamic interactions in nanopores and entropic traps. We report on electrophoretic mobilities, trapping times and translocation times and quantify the chain transition from free flowing behavior to trapping behavior in terms of the electric field strength.

Keywords: *mesoscale DNA dynamics, fluctuating hydrodynamics, frictional force coupling, entropic traps, pore translocation*

1 Model description

In the following model, the solvent is treated as a continuum isothermal, incompressible Newtonian fluid governed by Stokes (creeping) flow equations, while the solute particles, coupled to the fluid, follow Newton's second law of motion with additional stochastic terms. In contrast to computationally-intensive direct numerical simulation (DNS) methods, where the flow around a particle is fully resolved and the resulting forces obtained by integrating the stress fields over particle the surface, here the no-slip boundary condition at the particle surface is taken to give rise to a Langevin-like hydrodynamic force, composed of Stokes drag force and stochastic Brownian force. While the idea of approximating the effect of solute on the fluid by spreading a semi-empirical force over the surrounding grid nodes rather than enforcing a detailed boundary condition has long been in use in the multiphase flow community (particularly in the framework of Immersed boundary methods [50]), the specific form of the force (a constant times the difference between fluid and particle velocities) appears in several mesoscale approaches, such as Brownian dynamics [17] or Stokesian dynamics [64]. Thus, the particles act as localized point sources in the continuum fluid and the fluid-particle coupling enforces momentum exchange. This type of solvent-solute interaction has been explored particularly in the context of a fluctuating Lattice-Boltzmann model (LBM) for the fluid [1, 2, 10]. We extend this approach to include more complicated domains and the effects of electric field, but describe the fluid directly by the fluctuating Navier-Stokes equation. The total force acting on each particle includes, in general, four types of contributions, arising from: the imposed electric field (electrophoretic and dielectrophoretic forces), the hydrodynamic solvent-solute coupling (Stokes drag and Brownian force), intra-molecular forces (spring force and excluded volume effects) and wall repulsion effects. The corresponding fields are resolved on overlapping, finite-difference grids. These logically rectangular grids represent a compromise between structured and unstructured grids: while retaining good performance of a structured grid, they offer more flexibility over Cartesian or multi-block grids and adequately resolve boundary layers (such as the electric double layer).

*email: hotmape@eng.fsu.edu
†email: rchella@eng.fsu.edu

2 Hybrid model

We introduce the model for a coarse-grained polyelectrolyte chain in Sec. 2.1 and give the scales used throughout this work in Sec. 2.2. Equations of motion for the particles, Sec. 2.3, require solutions of the governing equations for the electric and hydrodynamic fields, discussed in Sec. 2.4 and 2.5. Sec. 2.6 describes the particle-fluid frictional coupling, whose full implementation requires renormalization of the friction coefficient, Sec. 2.7. For mathematical convenience and physical consistency, we transform the steady-state governing equations into their time-dependent forms, Sec. 2.9. The overall algorithmic implementation is detailed in Sec. 2.10.

2.1 Chain coarse-graining

Following [9] and [40], we interpret coarse-graining as averaging over irrelevant degrees of freedom (DOFs), the (ir)relevancy being based on the ratio of the characteristic time scale to the time over which the DOFs equilibrate. Slow variables are thus retained as essential features to ensure global accuracy while fast variables are in a quasi-steady state of equilibrium. A related concept of decimation is used in the renormalization group theory.

Bead-spring models of polymer chains, Fig. 1, constitute a compromise between finer-grained, yet stiffer, bead-rod models and rheological dumbbells. We use a coarse-grained bead-spring model, in which the beads represent points of solute-solvent interaction and the springs reflect the entropic forces that result from averaging of a finer-grained bead-rod model with rigid Kuhn rods as bead connectors. The chain is uniquely specified by the following set of parameters: the contour length L, number of springs N_s (or, equivalently, number of beads N), Kuhn length b_k and bead radius a. Related variables that can be derived from the above set and will be used throughout this work are maximum spring extension $q_0 = L/N_s$, number of Kuhn segments per spring $N_{ks} = q_0/b_k$ and root mean square (RMS) spring extension $R_s = b_k\sqrt{N_{ks}}$, with k_b the Boltzmann constant, K_s the spring constant and T the temperature.

The admissible range for the number of springs N_s varies over a bounded interval; since each spring corresponds to one normal mode, the lower bound is determined by the highest frequency of motion we wish to capture, ω, so that the relaxation time $\tau_{N_s} < \omega^{-1}$. The upper bound arises due to the assumption of a sufficiently long random walk (with step size equal to Kuhn length) in the derivation of spring force laws; [71] suggests $N_s < 0.1N_k$, where N_k is the number of Kuhn steps. The remaining parameters, namely Kuhn length b_k, bead radius a and excluded-volume interaction factor v are determined by matching the radius of gyration, longest relaxation time and diffusion coefficient to the experimental values, as was done in [34]; we employ the same values for our benchmark chain in simulations.

2.2 Non-dimensionalization

The equations used in this work are non-dimensionalized – as indicated by the hat symbol – in a self-consistent manner. The three fundamental scales used are length L_0 (characteristic geometry dimension H in confinement and particle radius a or maximum spring extension q_0 in free space), time T_0 (diffusive, L^2/D) and force F_0 (thermal, k_bT/L_0). The derived scales include electric potential ϕ_0 (intrinsic ζ_w and applied $\phi_{max,app}$), electric field strength E_0 ($\phi_{max,app}/L_0$), velocity U_0 (L_0/T_0), pressure P_0 ($U_0\eta/L_0$) and friction coefficient ζ_0 (F_0/U_0), where $\zeta = 6\pi\eta a$ is the friction coefficient, ρ solvent density, η viscosity, D diffusion coefficient, ζ_w wall zeta potential (located at the shear plane of the electric double layer) and $\phi_{max,app}$ the maximum applied potential.

2.3 Particle dynamics

The equations of motion for the i^{th} bead of mass m are given by

$$\begin{aligned} \frac{d\mathbf{r}_i}{dt} &= \mathbf{v}_i, \\ m\frac{d\mathbf{v}_i}{dt} &= -\zeta\left[\mathbf{v}_i(t) - \mathbf{U}(\mathbf{r}_i,t)\right] + \mathbf{F}_i^B(t) + \mathbf{F}_i^{NH}(t). \end{aligned} \tag{1}$$

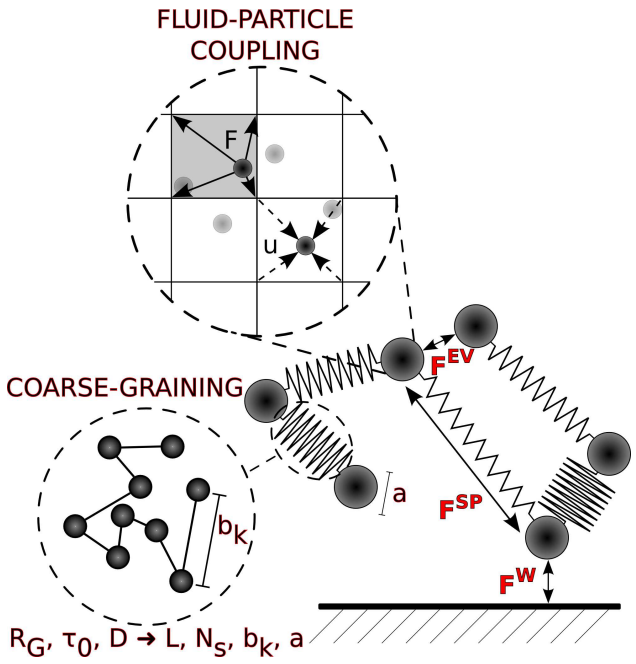

Fig. 1: Bead-spring model.

The Brownian force $\mathbf{F}_i^B(t)$ is derived from the fluctuation-dissipation theorem and averaged over a time interval dt,

$$\mathbf{F}^B(t) = \left(\frac{6k_bT\zeta}{dt}\right)^{0.5} \cdot \mathbf{n}(t). \tag{2}$$

The Wiener increments are represented by the components of the random vector $\mathbf{n}$, which have Gaussian distribution with zero mean and unit variance [40]. It should be noted that we are effectively solving the general, non-linear and non-Markovian Langevin equation. The dynamics, however, is studied here only with times much larger than the relaxation time scale, m/ζ, in which case the memory function reduces to the friction coefficient ζ. The effects of the Gaussian force, Eq. (2), can thus be given by its first and second moment [76],

$$\begin{aligned} \left\langle F^B(t)\right\rangle &= 0, \\ \left\langle F^B(t)F^B(t')\right\rangle &= 2k_bT\zeta\delta(t-t'), \end{aligned} \tag{3}$$

where $F^B(\cdot)$ is a one-dimensional component of the random force and $\delta(t-t')$ is the Dirac delta function, which indicates absence of correlations in the force between any distinct time intervals dt and dt'.

$\mathbf{U}(\mathbf{r}_i,t)$ is the total fluid velocity at particle location $\mathbf{r}_i$, which can be decomposed into the base, unperturbed velocity field (see Sec. 2.5) and a velocity disturbance field $\mathbf{u}'$, arising due to the perturbations from particles (see Sec. 2.6), i.e. $\mathbf{U} = \mathbf{u} + \mathbf{u}'$. At the same time, $\mathbf{U}(\mathbf{r}_i,t)$ is a mathematically convenient construct, which extrapolates the continuous fluid velocity field to the bead center. This velocity includes self-interaction, i.e. the deviation of the streamlines around the bead due to the bead itself, along with the effects of other particles, mediated by vorticity diffusion. Such velocity is not physically correct [39], although the error appears negligible yet difficult to quantify precisely. In addition, the self-interaction contribution contains an artifact of grid spacing; while there is formally an essential singularity in the Stokeslet at the source point, the method instead assigns a finite velocity to the source. This is because on a lattice with finite spacing, the Dirac delta function appearing in the force coupling described in Sec. 2.6 is smeared rather than localized. Renormalization of the friction coefficient, discussed in Sec. 2.7, attempts to address both of these issues.

The total non-hydrodynamic force contains, in general, contributions from the electrophoretic, dielectrophoretic, spring, excluded-volume and wall forces, respectively, i.e.

$$\mathbf{F}^{NH} = \mathbf{F}^{EP} + \mathbf{F}^{DEP} + \mathbf{F}^{SP} + \mathbf{F}^{EV} + \mathbf{F}^{W}. \tag{4}$$

Assuming a thin electric double layer (EDL) on the particle surface, neglecting polarization and retardation effects and using the point-dipole approximation, the electrophoretic and dielectrophoretic forces are given by [36],

$$\mathbf{F}^{EP} = 6\pi\zeta_p \epsilon a \mathbf{E}, \tag{5}$$

$$\mathbf{F}^{DEP} = -\pi\epsilon a^3 \nabla |\mathbf{E}|^2, \tag{6}$$

where ζ_p is surface potential on the particle and ϵ the fluid permittivity. Since the point dipole model neglects particle size, Eq. (6) is only approximate as it neglects higher order multipoles. Such an assumption is consistent with the force-coupling model and, furthermore, Hu [31] notes that the error is negligible as long as $a \ll H$. Nevertheless, we examine the effects of higher order multipole corrections on dielectrophoresis in Appendix A. Eq.(6) additionally assumes insulating particles in DC fields, for which the Clausius-Mossotti factor, $K_{CM} \equiv (\sigma_p - \sigma_f)/(\sigma_p + 2\sigma_f)$, where σ_p and σ_f are electrical conductivities of particle and fluid, respectively, reduces to -1/2.

The bonded force is modeled by the Marko-Siggia spring law [31], which describes well the semiflexible rigidity of a worm-like chain such as DNA. The spring force exerted on bead i by spring i is

$$\mathbf{F}_i^{SP} = \frac{k_b T}{2 b_k} \left(\left(1 - \frac{R_i}{q_0} \right)^{-2} - 1 + 4 \frac{R_i}{q_0} \right) \frac{\mathbf{R}_i}{R_i}, \tag{7}$$

where the spring vector $\mathbf{R}_i \equiv \mathbf{r}_{i+1} - \mathbf{r}_i$ and the inter-bead distance $R_i = |\mathbf{R}_i|$.

For a solvent far away from θ-temperature, excluded-volume interactions (EVs) need to be included. Pair-wise EVs between beads i and j are short-ranged and can thus be approximated by the delta function,

$$U_{ij}^{EV} \approx v k_b T \delta \left(\mathbf{R}_{ij} \right), \tag{8}$$

with $\mathbf{R}_{ij} \equiv \mathbf{r}_i - \mathbf{r}_j$, $R_{ij} = |\mathbf{R}_{ij}|$ and v the interaction volume parameter [60]. The delta function can, in turn, be approximated by a Gaussian potential, which is a common starting point when developing computational implementations. Jendrejack's potential [34], which is softer than the traditional Lennard-Jones and is based on Öttinger's work [53], is particularly suitable for our purpose as it depends on the root-mean-square spring extension and thus reflects the details of coarse-graining. Upon taking negative gradient of the potential, we obtain the force on bead i in the form

$$\mathbf{F}_i^{EV} = \sum_{j=1}^{N} \frac{243\, v k_b T}{4\sqrt{2}\pi^{3/2}\, b_k^4 R_s} \exp\left(-\frac{9 R_{ij}^2}{2 R_s^2} \right) \mathbf{R}_{ij}. \tag{9}$$

The bead-wall repulsion is modeled by a potential suggested by Jendrejack [34], proportional to the cubic power of the bead-wall distance and active only within boundary layer of thickness δ_w,

$$U_i^W = \begin{cases} \frac{A_w}{3\, b_k\, \delta_w^2} \left(D_i - \delta_w \right)^3 & \text{if } D_i < \delta_w \\ 0 & \text{if } D_i \geq \delta_w, \end{cases} \tag{10}$$

where D_i is the normal distance of i bead from the nearest wall. The corresponding force is

$$\mathbf{F}_i^W = \begin{cases} \frac{-A_w}{b_k\, \delta_w^2} \left(D_i - \delta_w \right)^2 \nabla D_i & \text{if } D_i < \delta_w \\ \mathbf{0} & \text{if } D_i \geq \delta_w, \end{cases} \tag{11}$$

The parameter A_w regulates the strength of the force and is typically on the order of $O(k_b T)$. If too small, the beads may penetrate walls when large forces or velocity gradients are encountered. If too large, the chain motion becomes unphysically retarded by the dominant wall force and will not obey the relevant scaling laws.

Respecting the order of magnitude estimate, we thus assign it the lowest value that prevents wall penetration. For the choice of δ_w we may find some guidance in [45], which reports that in slow flows the thickness of the depletion layer near the walls is roughly $3a$. The depletion layer is set up through the combined effect of steric hindrance and HIs. However, in confined flows, HIs become partially screened due to nearby no-slip walls; the dominance of steric effects thus suggests $\delta_w \sim a$. Alternative techniques of incorporating wall effects have been used, such as repositioning a penetrating bead to the nearest wall [38] or representing the wall force as a linear superposition of several phenomenological contributions, including those due to electric double layer, van der Waals forces and steric effects [16].

Since the normal distance to the nearest wall (scaled by the geometry length scale H) can be viewed as a signed distance function $\hat{D}$, it can be efficiently found in complex geometries as the solution to the Eikonal equation

$$\begin{aligned} |\hat{\nabla}\hat{D}| &= 1 && \text{for } \mathbf{x} \in \Omega, \\ \hat{D} &= 0, && \text{for } \mathbf{x} \in \Gamma_W, \\ \hat{\nabla}\hat{D} \cdot \mathbf{n} &= 0, && \text{for } \mathbf{x} \in \Gamma_I \cup \Gamma_O, \end{aligned} \tag{12}$$

where $\mathbf{n}$ represents a unit normal to the surface, Ω is a bounded computational domain in $\mathbf{R}^3$, $\Gamma = \Gamma_W \cup \Gamma_I \cup \Gamma_O$ is the boundary of Ω, and Γ_W, Γ_I and Γ_O are boundary segments corresponding to the walls, inlet and outlet of the domain, respectively. Equation (12) is a special case of a general family of Hamilton-Jacobi equations, whose fast marching solution and suitable numerical Hamiltonians are discussed in [62]. However, if Neumann boundaries are present, as in our case, fast marching algorithms require modification, which results in decreased computational efficiency. As an alternative approach, we square Eq. (12) and convert the steady-state problem into an initial-value problem

$$\frac{d\hat{D}}{d\hat{t}} = -\left(\hat{\nabla}\hat{D}\right)^2 + \gamma\,\hat{\Delta}\hat{D} + 1 \qquad \text{for } \mathbf{x} \in \Omega, \tag{13}$$

where $\gamma > 0$. Explicit time-stepping (the 4-step Adams-Bashforth method started with the 4th order Runge-Kutta method) is applied until steady-state is achieved. While $\hat{D}$ is continuous, its gradient satisfies a conservation law that can develop shocks, and thus is expected to be discontinuous. To stabilize our central difference scheme, we add artificial dissipation, which corresponds to the second term on the right hand side of Eq. (13). Stabilization based on even-order derivatives is frequently encountered in numerical solutions of hyperbolic equations, cf. Lax-Friedrichs and Lax-Wendroff schemes. As an added benefit of this approach, tuning γ may allow one to take into account the curvature of the bounding surfaces, e.g. by reducing or increasing the normal distance around concave or convex corners [18]. While wall repulsion is only active within a finite boundary layer adjacent to the walls of the bounding geometry, we want to retain the option of changing the boundary layer thickness without having to recompute the distance function. Consequently, the underlying grid on which the Eq. (13) is solved consists of a coarse background grid and fine, overlapping boundary layer grids.

In the presence of walls in the domain, the distance function and its derivatives are needed at each time step. To expedite access to these variables, they are pre-processed into a data structure (kd-tree), which is then used to perform an approximate nearest neighbor (ANN) search, outlined in [5]. After the search, the current location of the bead i is mapped to the nearest gridpoint at which the values of $\hat{D}$ and $\hat{\nabla}\hat{D}$ are available.

Most systems exhibit large separation of the inertial and diffusive time scales, $m/\zeta \ll L^2/D$; e.g. for a micron particle in water at room temperature, the separation is of the order of $O(10^4)$ [42]. We can then integrate the Langevin equation, Eq. (1), over the inertial time scale, arriving at a typical Brownian dynamics representation. The acceleration term in Eq. (1) vanishes and the condition of force balance follows.

2.4 Electric field

We use a linearized Poisson-Boltzmann equation for the electric potential, which results from the Debye-Hückel approximation. Due to the numerical approach employed, this approximation is, however, non-essential and can be relaxed if walls with high surface potentials need to be modeled. The total potential

is split into a linear superposition of the intrinsic potential ϕ_i (due to wall charge) and applied potential ϕ_a (due to the externally imposed electric field), $\phi = \phi_i + \phi_a$, yielding Helmholtz and Poisson equations, respectively:

$$\begin{aligned}
\hat{\nabla}^2\hat{\phi}_i &= \hat{\kappa}^2\hat{\phi}_i, && \text{for } \mathbf{x} \in \Omega, \\
\hat{\nabla}\hat{\phi}_i \cdot \mathbf{n} &= 0, && \text{for } \mathbf{x} \in \Gamma_I \cup \Gamma_O, \\
\hat{\phi}_i &= \hat{\zeta}_w, && \text{for } \mathbf{x} \in \Gamma_W, \qquad (14)
\end{aligned}$$

$$\begin{aligned}
\hat{\nabla}^2\hat{\phi}_a &= 0, && \text{for } \mathbf{x} \in \Omega, \\
\hat{\phi}_a &= \hat{\phi}_{max,app}, && \text{for } \mathbf{x} \in \Gamma_I \cup \Gamma_O, \\
\hat{\nabla}\hat{\phi}_a \cdot \mathbf{n} &= 0, && \text{for } \mathbf{x} \in \Gamma_W. \qquad (15)
\end{aligned}$$

The gradient operator and the inverse Debye length κ are scaled by L_0. The potentials appear in the body force acting on the fluid and in the electrophoretic and dielectrophoretic forces acting on the particles, which are proportional to the electric field strength $\mathbf{E} = -\nabla\phi_a$ and $\nabla|\mathbf{E}|^2$, respectively. Since the gradient of the intrinsic potential is dominant only in a thin EDL adjacent to the walls, its contribution to $\mathbf{E}$ is neglected.

2.5 Unperturbed fluid velocity and pressure fields

The incompressible, steady-state Navier-Stokes equations for a solvent of density ρ are tackled in the primitive variables formulation. If an external electric field is imposed, the right-hand side will contain an additional, Korteweig-Helmholtz electric body force given by the divergence of the Maxwell stress tensor as $\mathbf{f} = \rho_f\mathbf{E} = -\rho_f\nabla\phi_a$, with the effects due to electrostriction and non-uniform permittivity neglected, yielding

$$\rho\,\mathbf{u}\cdot\nabla\mathbf{u} + \nabla p - \eta\nabla^2\mathbf{u} = \mathbf{f}, \quad \nabla\cdot\mathbf{u} = 0 \qquad \text{for } \mathbf{x} \in \Omega, \qquad (16)$$

where the volumetric free charge density $\rho_f = -\epsilon\kappa^2\phi_i$ follows from Eq. (14). After non-dimensionalization, we have

$$\begin{aligned}
\mathrm{Re}\,\hat{\mathbf{u}}\cdot\hat{\nabla}\hat{\mathbf{u}} + \hat{\nabla}\hat{p} - \hat{\nabla}^2\hat{\mathbf{u}} &= \hat{\mathbf{f}}, && && (17) \\
\hat{\nabla}\cdot\hat{\mathbf{u}} &= 0, && \text{for } \mathbf{x} \in \Omega, && (18) \\
\hat{\mathbf{u}} &= 0 \quad \text{(no slip)}, && \text{for } \mathbf{x} \in \Gamma_W, && (19) \\
\hat{\nabla}\hat{\mathbf{u}}\cdot\mathbf{n} &= 0 \quad \text{(free stream)}, && \text{for } \mathbf{x} \in \Gamma_I \cup \Gamma_O, && (20)
\end{aligned}$$

where $\hat{\mathbf{f}} = C_e\hat{\phi}_i\hat{\nabla}\hat{\phi}_a$, $C_e = \hat{\kappa}^2\hat{u}_{HS}$, Helmholtz-Smoluchowski characteristic velocity $u_{HS} = -\epsilon\zeta_w E_0/\eta$ and Reynolds number $\mathrm{Re} = \rho U_0 L_0/\eta$. For microscale geometries, $\mathrm{Re} \to 0$, so the convective term in Eq. (17) vanishes, reducing the system to the creeping flow model. To reformulate the boundary value problem in terms of the pressure-Possion system, we generate a Poisson equation for the pressure by taking the divergence of the momentum equation (17) and using the incompressibility condition (18). Following Henshaw [28], we also add a penalty term proportional to the velocity divergence,

$$\alpha(\mathbf{x})\nabla\cdot\mathbf{u},$$

to dampen out pressure oscillations arising from the use of central finite difference formulas on a collocated grid. To derive a boundary condition for pressure, the normal component of the momentum equation is typically applied on the boundary [25]. Such boundary condition is insufficient [28], however, and needs to be supplemented by the incompressibility constraint, $\delta \equiv \nabla\cdot\mathbf{u} = 0$. Alternatively, the normal derivative of the velocity divergence can be required to vanish at the boundary, $\partial\delta/\partial n$, yielding a curl-curl boundary condition [56] for the pressure. The resulting pressure equation thus adopts the form of

$$\begin{aligned}
\hat{\nabla}^2\hat{p} - \hat{\alpha}\hat{\nabla}\cdot\hat{\mathbf{u}} &= \hat{\nabla}\cdot\hat{\mathbf{f}}, && \text{for } \mathbf{x} \in \Omega, && (21) \\
\frac{\partial\hat{p}}{\partial\mathbf{n}} &= -\mathbf{n}\cdot\nabla\times\nabla\times\hat{\mathbf{u}} + \mathbf{n}\cdot\hat{\mathbf{f}}, && \text{for } \mathbf{x} \in \Gamma, && (22)
\end{aligned}$$

where $\hat{\nabla}\cdot\hat{\mathbf{f}} = C_e\hat{\nabla}\hat{\phi}_i\hat{\nabla}\hat{\phi}_a$. The elliptic equation for the pressure, Eq. (21)-(22), thus replaces the continuity equation, Eq. (18). The factor $\hat{\alpha}$ is set to a constant, $(L_0/\Delta x)^2$, where Δx is an average grid spacing.

2.6 Fluid-particle coupling

The momentum transfer between a particle and the fluid is introduced through a Langevin-like particle force that is assumed to have the following form [1],

$$\mathbf{F}_i^{prt}(\mathbf{r}_i, t) = -\zeta_{eff}\left[\mathbf{v}_i(t) - \mathbf{U}(\mathbf{r}_i, t)\right] + \mathbf{F}_i^B(t). \tag{23}$$

The effective friction ζ_{eff} can be estimated by a systematic procedure discussed in Sec. 2.7. Based on the deterministic and stochastic simulations [1] performed with this method, we expect that the Brownian force (last term on the right hand side of Eq. (23)) can be neglected if thermal fluctuations in the fluid are to be left unresolved. We will thus refer to Eq. (23) with only the Stokes drag term (first term on the right-hand-side) as reduced coupling, as opposed to the full coupling of Eq. (23).

While the conceptual idea of force coupling has been employed within the last three decades in e.g. Brownian dynamics, Immersed boundary method or coupled Langevin equations approach [54], a rigorous treatment of the specific form given by Eq. (23) has been pioneered only recently, mostly in the context of a Lattice-Boltzmann fluid [1, 2, 10]. The main goal of this concept is to capture the velocity-dependent HIs with a reasonable compromise between accuracy and computational efficiency.

Practitioners of force coupling implicitly assume it to be instantaneous; in other words, there is large time scale separation required between momentum transfer and chain diffusion [10, 45], i.e. the Schmidt number

$$Sc = \frac{\nu}{D} \gg 1, \tag{24}$$

where ν is kinematic viscosity. This is typically achieved for micron-scale structural units immersed in aqueous solvent at room temperature [42], thus allowing one to neglect the influence of the shape of the particles on the disturbance fields and treat the particles as point masses. None of these assumptions are, however, essential for the model to remain valid. The effect of larger particles can be partially accounted for by using regularized delta functions, typically in the form of radial basis functions [41] or regularized Stokeslets [15]. Small Schmidt numbers (e.g. for short chains), on the other hand, will require unsteady Stokes flow description. This is because large diffusion coefficients restrict the time step ($\Delta t < \tau_D \approx R_g^2/D$, R_g is the radius of gyration of the chain), thereby increasing the frequency of the forcing. This in turn leads to large Reynolds to Strouhal number ratio, $Re/Sr = R_g^2/(\nu\Delta t)$, necessitating presence of the time derivative in the Stokes equation. The inclusion of the inertial term also frees us from the assumption of large particle density (compared to the fluid).

Based on the above considerations, we can rewrite the Navier-Stokes equation (16) in a time-dependent form,

$$\rho\frac{\partial \mathbf{U}}{\partial t} + \nabla p - \eta\nabla^2\mathbf{U} = \mathbf{f}^{tot}, \quad \nabla\cdot\mathbf{U} = 0, \tag{25}$$

with the advection term $\mathbf{U}\cdot\nabla\mathbf{U}$ neglected in the low Reynolds number limit. We have also added additional force densities; the total force density acting on the fluid at a field point $\mathbf{r}$, $\mathbf{f}^{tot}(\mathbf{r})$, now contains contributions from the base field (electric field) $\mathbf{f}$, fluid-particle coupling $\mathbf{f}^{prt}$ and thermal fluctuations in the fluid $\mathbf{f}^{thm}$, yielding

$$\mathbf{f}^{tot}(\mathbf{r}, \mathbf{R}, t) = \mathbf{f}(\mathbf{r}) + \mathbf{f}^{prt}(\mathbf{r}, \mathbf{R}, t) + \mathbf{f}^{thm}(\mathbf{r}, t), \tag{26}$$

thus acquiring a form similar to that of the stochastic immersed boundary method [7]. Denoting the $3N$ vector of all bead positions $\mathbf{r}_i$ as $\mathbf{R}$, Eq. (26) explicitly emphasizes the dependence of the particle force density $\mathbf{f}^{prt}$ on the bead positions, coupling the Langevin equation and the Navier-Stokes equation; a specific implementation of the solution to such coupled system is discussed in Sec. 2.10. In analogy with linear splitting of the total velocity field into the superposition of the base and perturbation fields, $\mathbf{U} = \mathbf{u} + \mathbf{u}'$, we define

$$\mathbf{f}' = \mathbf{f}^{prt} + \mathbf{f}^{thm}, \tag{27}$$

as the force density inducing the corresponding perturbation flow $\mathbf{u}'$. The coupling force density follows

naturally from Eq. (23) as

$$\mathbf{f}^{prt}(\mathbf{r},\mathbf{R},t) = -\sum_{i=1}^{N}\left\{\zeta_{eff}\left[\mathbf{U}(\mathbf{r}_i,t)-\mathbf{v}_i(t)\right]+\mathbf{F}_i^B(t)\right\}\delta(\mathbf{r}-\mathbf{r}_i) \tag{28}$$

$$= -\sum_{i=1}^{N}\mathbf{F}_i^{prt}\delta(\mathbf{r}-\mathbf{r}_i), \tag{29}$$

where the thermal fluctuations $\mathbf{f}^{thm}(\mathbf{r},t)$, described in Sec. 2.8, need to be included to satisfy the fluctuation-dissipation theorem [2, 54, 39]. By finding a stationary solution of the Fokker-Planck equation associated with the system of Eqs. (1) (with $\mathbf{F}^{NH}=0$) and (25), it can be shown [1] that the presence of $\mathbf{f}^{thm}$ in Eq. (26) is needed for the full coupling to satisfy the fluctuation-dissipation theorems for the particle-fluid system. We note that for unbounded flow, the over-damped limit of the Langevin equation (1) with the coupling described above is equivalent to the Brownian dynamics scheme [17], provided we drop the hydrodynamic interaction tensors and replace the homogeneous flow field of the solvent with a more accurate $\mathbf{U}$. In addition, if $\mathbf{f}^{tot}=\mathbf{f}^{prt}$, the free-space Green's function of the singularly forced Eq. (25) can be obtained analytically, either by Laplace transform [57] or by analogy with the fundamental solution of the unsteady heat equation [13].

While mathematically self-consistent, the coupling is only an approximate replacement of the no-slip boundary condition at the surface of rigid objects, with the error growing with the decreasing time and length scales [1]. There are two additional physical issues with this coupling [39]: first, the friction is not strictly Markovian; this, however, has little effect on the long-time dynamics we are interested in. Second, as mentioned in Sec. 2.3, the fluid velocity field $\mathbf{U}$ necessarily includes self-interaction, which will underestimate the drag force. This can be partially remedied by renormalizing the friction coefficient and adopting ζ_{eff} (Sec. 2.7).

2.7 Friction renormalization

The bare friction coefficient ζ needs to be renormalized for HI simulations to account for lattice discretization. A simple procedure [10] assumes an effective friction ζ_{eff} in the form of

$$\frac{1}{\zeta_{eff}} = \frac{1}{\zeta} + \frac{g}{\eta\Delta x}, \tag{30}$$

where the constant g can be obtained as follows. We apply a point force $\mathbf{F}$ and measure the velocity at the origin of the force, $\mathbf{u}(0)$. Since the ratio of that velocity to the applied force should be equal to the Green's function of the Stokes flow, which is inversly proportional to the viscosity and the distance between the source point and the observation point, we expect

$$\frac{\mathbf{u}(0)}{\mathbf{F}} = \frac{g}{\eta\Delta x}. \tag{31}$$

2.8 Fluctuating hydrodynamics

Efficient solutions of the Landau-Lifshitz Navier-Stokes equations (LLNS) are an area of active research, with exponential integrators in Fourier space [7] and modified Runge-Kutta methods [72] showing promise. To account for thermal fluctuations in LLNS, the right-hand-side of Navier-Stokes equation is augmented by the divergence of stochastic flux tensor, $\mathbf{f}^{thm}=\nabla\cdot\mathbf{S}$, with zero mean and covariance given by [8]

$$\left\langle \mathbf{S}_{ij}\left(\mathbf{r},t\right)\mathbf{S}_{kl}\left(\mathbf{r}',t'\right)\right\rangle = 2k_bT\eta\left(\delta_{ik}\delta_{jl}+\delta_{il}\delta_{jk}-\frac{2}{3}\delta_{ij}\delta_{kl}\right)\delta(\mathbf{r}-\mathbf{r}')\delta(t-t'), \tag{32}$$

where subscripted δ is a Kronecker delta.

For an isothermal fluid, the components of $\mathbf{S}$ can thus be written as

$$\mathcal{S}_{mn} = \sqrt{\frac{2k_bT\eta}{\Delta t\Delta V_c}\left(1+\frac{1}{3}\delta_{mn}\right)}\cdot\mathcal{R}_{mn}, \qquad \text{for } m,n=\{1,2,3\}, \tag{33}$$

where V_c is the volume of a cell over which the fluctuations are discretized and $\mathcal{R}_{mn}$ are independent and identically distributed Gaussian random variables with zero mean and unit variance. Since $\mathbf{S}$ is a symmetric dyad, it can be split into a symmetric traceless part and an isotropic part, $\mathbf{S} = C(\sqrt{4/3}\,\mathbf{I} + \mathbf{1})\,\mathbf{R}$, where the constant C along with the contributing tensors follow from Eq. (33). Six independent random numbers are thus needed per cell per time step to generate the required Gaussian random field discretized on the lattice.

It has been shown that the discrete system produced by central differencing will not always be thermodynamically consistent and correction terms may be needed [61]. In addition, representing the fluctuations, which are delta function-correlated in time, by Δt^{-1} scaling (Eq. (33)) seems reasonable only if Δt is smaller than the shortest relaxation time in the system [39]. Spatial discretization is a compromise among various factors; while we generally prefer to minimize the grid spacing to be able to resolve large field gradients and reduce the truncation error of the finite difference scheme, the assumptions of a constant density and constant temperature continuum fluid impose a lower bound on the grid spacing, which is on the order of 0.1 μm for physiological fluids [39]. The point force model of particles imposes a similar constraint.

2.9 False transients

For computational efficiency, the elliptic systems (14)-(15),(17)-(22) and (12) are parabolized (such a technique is known under various names, e.g. method of pseudotransients [66] or false transients [46]). To illustrate the concept that was already applied in Eq. (13), we note that the transformed Navier-Stokes system (17) and (21) adopts the following form:

$$\frac{\partial \mathbf{\Theta}}{\partial \tau} = L\mathbf{\Theta} + G, \tag{34}$$

where

$$\mathbf{\Theta} = \begin{bmatrix} \hat{\mathbf{u}} \\ \hat{p} \end{bmatrix}, \quad L = \begin{bmatrix} \hat{\nabla}^2 & -\hat{\nabla} \\ -\hat{\alpha}\hat{\nabla}\cdot & \hat{\nabla}^2 \end{bmatrix}, \quad G = \begin{bmatrix} \hat{\mathbf{f}} \\ -\hat{\nabla}\cdot\hat{\mathbf{f}} \end{bmatrix}. \tag{35}$$

The steady-state solution (where the time derivative vanishes identically) to the parabolized system represents the solution to the original system. The artificial time τ plays the role of an iteration parameter, which can be modified to accelerate convergence; the system now also lends itself to various operator splitting techniques that can further improve stability and accuracy. As an estimate of the upper bound for the timestep $\Delta\tau$ we use the result of the von-Neumann stability analysis for the 3D diffusion equation, $\Delta\tau \leq (\Delta x)^2/6$. If the original problem is already time-dependent (as in the case of Eq. (25)), τ becomes the real time t. This approach thus unifies the solution methodology for the steady and unsteady state problems that we encounter here.

2.10 Algorithm details

The base velocity and pressure fields are independent of the bead positions and thus precomputed in advance, Eq. (16). When time-stepping through the particles' equations of motion, Eq. (1), at regular intervals (depending on the required accuracy) we extrapolate the coupling force (Eq. (23)) from the particle position to the neighboring grid points, rescale it, update the total force density $\mathbf{f}^{tot}$ (Eq. (26)) and resolve the momentum equation (25) for the perturbed velocity and pressure fields subject to the same boundary conditions as for the unperturbed fields (Sec. 2.5). Whenever a field value, such as fluid velocity or electric field strength, is needed at the particle location, we interpolate it from the neighboring grid nodes using trilinear interpolation. The same interpolation is used for distributing the hydrodynamic force back to the fluid so as to satisfy Newton's 3rd law.

Hereafter we drop the hats to simplify notation, assuming all variables are non-dimensional, and summarize the steps to solve the system coupling fluid and particle dynamics. Written in a general form explicitly indicating dependences on the perturbation velocity $\mathbf{u}'$ and the $3N$ vector of bead positions $\mathbf{R}$, we have a

coupled system of Langevin equation for the particles,

$$m\frac{d^2\mathbf{R}}{dt^2} = \mathbf{F}^{prt}\left(\mathbf{R}(t), \mathbf{u'}_{SS}(t)\right) + \mathbf{F}^{NH}\left(\mathbf{R}(t)\right), \tag{36}$$

$$\mathbf{R}(0) = \mathbf{R}_0, \quad \frac{d\mathbf{R}}{d\mathbf{t}}(0) = \mathbf{V}_0, \tag{37}$$

$$\mathbf{u'}_{SS}(0) = 0, \tag{38}$$

and Navier-Stokes equations for the velocity and pressure disturbance fields, $\mathbf{u'}$ and p', respectively,

$$\frac{\partial \mathbf{\Theta'}}{\partial \tau} = L\mathbf{\Theta'} + G', \quad \mathbf{\Theta'} = \begin{bmatrix}\mathbf{u'}(\tau,t)\\ p'(\tau,t)\end{bmatrix}, \quad G' = \begin{bmatrix}\mathbf{f'}(\mathbf{R}(t), \mathbf{u'}_{SS}(t))\\ -\nabla\cdot\mathbf{f'}(\mathbf{R}(t), \mathbf{u'}_{SS}(t))\end{bmatrix}, \tag{39}$$

$$\mathbf{u'}(0,t) = \begin{cases} \mathbf{u'}_{SS}(0) & \text{for } t = 0\\ \mathbf{u'}_{SS}(t-\Delta t) & \text{for } t > 0,\end{cases} \tag{40}$$

where the perturbation force density $\mathbf{f'}$ follows from Eq. (27), the steady-state velocity is defined as

$$\mathbf{u'}_{SS}(t) \equiv \mathbf{u'}(t) = \left\{\mathbf{u'}(\tau,t) : \frac{\partial \mathbf{u'}(\tau,t)}{\partial \tau} = 0\right\}, \tag{41}$$

the initial particle velocities $\mathbf{V}_0$ are drawn from the Maxwell-Boltzmann distribution and $\mathbf{F}$ represents the $3N$ vector of the corresponding bead forces $\mathbf{F}_i$.

To solve the coupled system of Eqs (36)-(40) at discrete times t_n for $n \in [0, \ldots N_t - 1]$, where N_t is the number of time steps, we iterate through the following predictor-corrector cycle at each time step:

1. Solve, off the lattice, the Langevin system Eq. (36)-(38) with $\mathbf{F}^{prt}_n = \mathbf{F}^{prt}(\mathbf{R}_n, \mathbf{u'}_{SS,n})$ to obtain $\mathbf{R}_{n+1}$.
2. Predict the particle force $\mathbf{F}^{prt}_*(\mathbf{R}_{n+1}, \mathbf{u'}_{SS,n})$ and extrapolate to neighboring lattice nodes, Eq. (28).
3. Solve, on the lattice, the Navier-Stokes system Eq. (39)-(40) with $\mathbf{f}^{prt}_*$ to obtain $\mathbf{u'}_{SS,n+1}$.
4. Interpolate the velocity perturbation to bead locations and correct the particle force $\mathbf{F}^{prt}_{n+1}(\mathbf{R}_{n+1}, \mathbf{u'}_{SS,n+1})$.

This approach allows us to cover the entire range of Schmidt numbers by letting Eq. (39) model either steady or unsteady Stokes flow. For the latter, we interpret τ as the real time rather than an artificial iteration parameter and thus redefine Eq. (41) as

$$\mathbf{u'}_{SS}(t) \equiv \{\mathbf{u'}(\tau,t) : \tau = t\}. \tag{42}$$

Stability of Eq. (39) typically allows us to take $\Delta\tau = \Delta t$ and thus step 3 of the above algorithm only needs one time step. For large Schmidt numbers, the $\mathbf{\Theta'}$ field will respond almost instantaneously to the redistribution of the beads between the successive time steps and the solutions to the steady and unsteady Stokes equations coincide.

The Langevin equation was integrated with the velocity Verlet method [21] – a fast, stable, 2nd order accurate symplectic integrator developed originally for Hamiltonian systems. The Navier-Stokes equations are solved by the method of lines approach: the spatial discretization uses 4th order central difference formulas and two extra lines of ghost points while time-stepping is based on forward Euler method. As an alternative we tested a more efficient linear multistep method (4-step Adams-Bashforth started with the 4th-order Runge-Kutta method), but the stability region proved too restrictive for our purpose. The equations are discretized on structured, boundary-fitted overlapping grids. Steady-state elliptic problems are, upon discretization, solved by sparse direct (Yale) or iterative solvers (GMREs or multigrid), depending on the size of the problem.

3 Hybrid model validation

In Sec. 3.1 we specify the simulation parameters. To validate the hybrid model and the frictional coupling discussed in Sec. 2, we examine two direct manifestations of HIs: formation of depletion layers near solid

boundaries, Sec. 3.2, and long-time tails of the velocity autocorrelation function (VAF), Sec. 3.3. Further, indirect validation is sought in the context of bead-spring chain dynamics. First, we conduct bulk simulations of polymer relaxation, Sec. 3.4, and verify bulk scaling of the diffusion coefficient, radius of gyration and end-to-end distance with chain length, Sec. 3.5. Then, in Sec. 3.6, we discuss diffusion under confinement and re-visit depletion layers. Appendix A addresses dielectrophoretic (DEP) separation of biological cells, where we attempt to put a heuristic DEP correction factor, proposed in the literature, on a firmer ground by examining multipolar corrections to the DEP force.

3.1 Physical properties and model parameters

Unless otherwise indicated, we will take as our benchmark polyelectrolyte a λ-phage DNA, stained with an intercalating dye YOYO-1, with the following set of properties [40, 34]: 48,502 base pairs, molecular weight $M_w = 31.5 \times 10^6$ Daltons, contour length $L = 21$ μm, Kuhn length $b_k = 0.106$ μm, number of springs $N_s = 10$ and bead radius $a = 0.077$ μm.

The time step Δt should be smaller than the diffusive time for the polymer, $\Delta t < \tau_D = L^2/D$, where $D = k_bT/\zeta$ is the diffusion coefficient and the length scale L should reflect the size of the polymer. Further upper bound is placed on the time step by the use of Euler-like integration schemes employed in this work; reasonable accuracy is obtained provided the external force is slowly varying during a time interval of Δt. Based on these observations, we take $L^2 = S_s^2$, where $S_s^2 = q_0 b_k/6$ is the squared radius of gyration of an ideal chain, and use a timestep in the range $\Delta t = \left\langle 10^{-3}\tau_D, 10^{-2}\tau_D \right\rangle \sim \left\langle 10^{-5}, 10^{-4} \right\rangle$ s. The simulations are performed at room temperature in a 1 cP solvent and the results averaged over 100 realizations on a parallel computer cluster to achieve statistical significance.

3.2 Velocity disturbance near a plane wall

Bead-wall HIs, particularly prominent in the vicinity of a wall, will generate asymmetric flow patterns in the hydrodynamic disturbance field. These flows, in turn, affect chain migration. A prototypical example is the formation of depletion layers [45], studied in detail in [30]. Analytical treatment of simple distributions of point forces near a plane wall is traditionally based on the method of images [11], where the desired Green's function is decomposed into a free-space contribution and a collection of image singularities located outside the domain of flow. Green's functions for other simple geometries, including intersecting planes and circular pipes and cones, can be derived analogously [57].

Let us consider a dumbell positioned parallel to a plane wall located at $y = 0$, which is the average orientation of polymer chains in shear flows. Upon solving the Navier-Stokes equation (25) with the reduced coupling,

$$\mathbf{f}^{prt}(\mathbf{r}, t) = -\sum_{i=1}^{2} \left\{\zeta_{eff} \left[\mathbf{U}(\mathbf{r}_i, t) - \mathbf{v}_i(t)\right]\right\} \delta(\mathbf{r} - \mathbf{r}_i), \tag{43}$$

we obtain a velocity field whose contours, projected in the xy plane, are depicted in Fig. 2. We see that particles in the vicinity of the dumbell migrate away from the walls, depleting the region in the boundary layer, as predicted by the theory based on Blake's method [45]. Depletion layers are re-visited in Sec. 3.6 to further validate the model, this time in the context of bead-spring chains.

3.3 Long-time tails of velocity autocorrelation function

A straightforward way to check that HIs are, at least partially, resolved is to capture the long-time tail of the velocity autocorrelation function (VAF) of a single particle [1]. The tail signifies a power-law decay of VAF ($\propto t^{-3/2}$) in the long-time limit, as opposed to an exponential decay predicted by the Langevin theory. It was first reported based on molecular dynamics simulations [4] and is believed to be due to the diffusion of, and viscous dissipation in, a vortex associated with a moving particle. It can be derived rigorously from the Boltzmann equation with extended collision sequences [48] or mode-coupling theory [76].

Two sets of experiments were conducted. To minimize dependence of results on the mass and radius of the bead, we chose $\hat{m} = 1$ and $\hat{\zeta} = \zeta_c \cdot \hat{m}/\Delta\hat{t}$, with varying friction prefactor ζ_c. In the first, deterministic case, all

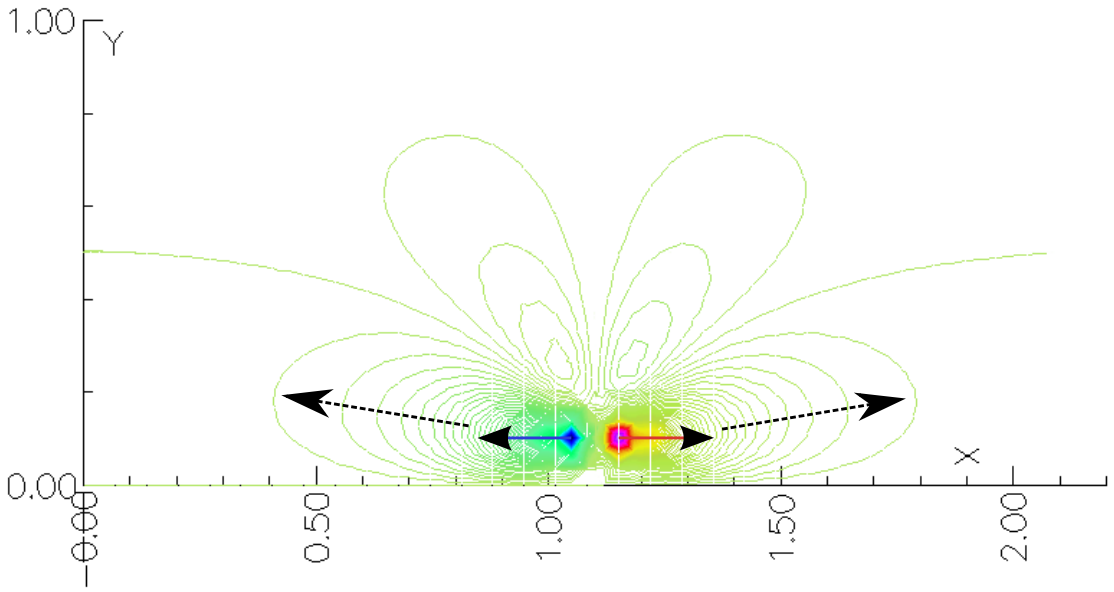

Fig. 2: Velocity contour lines of a disturbance field due to force dipole in the vicinity of plane wall. The solid arrows denote the opposing forces acting on the beads while the dashed arrows denote two representative velocity vectors in the vicinity of the force dipole.

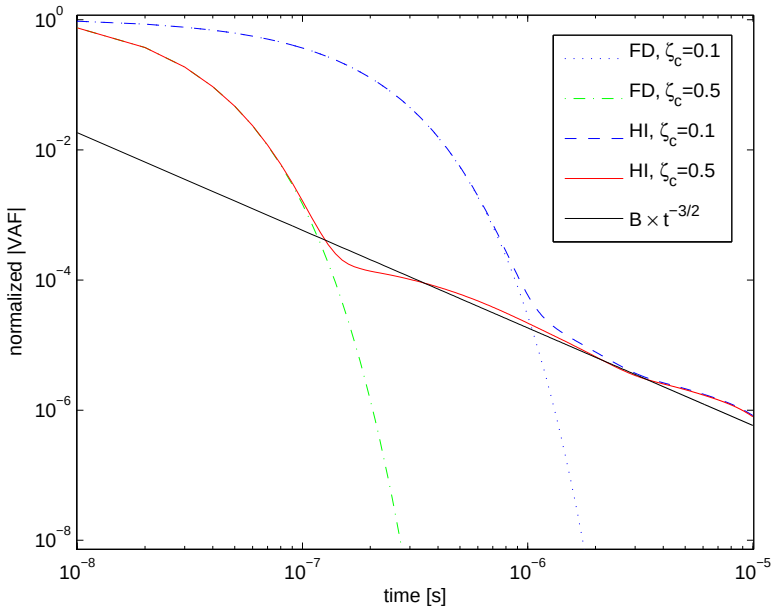

Fig. 3: Decay of velocity autocorrelation function - deterministic experiment. While the free-draining (FD, no force coupling included) data indicate exponential decay, the HI simulation (force coupling included), designed to recover effects of hydrodynamic interactions, captures the power-law tail. The power-law prefactor, $B = 1/12 k_b T \sqrt{\rho} \, (\pi\eta)^{-3/2}$ [14], is independent of the mass or size of the Brownian particle.

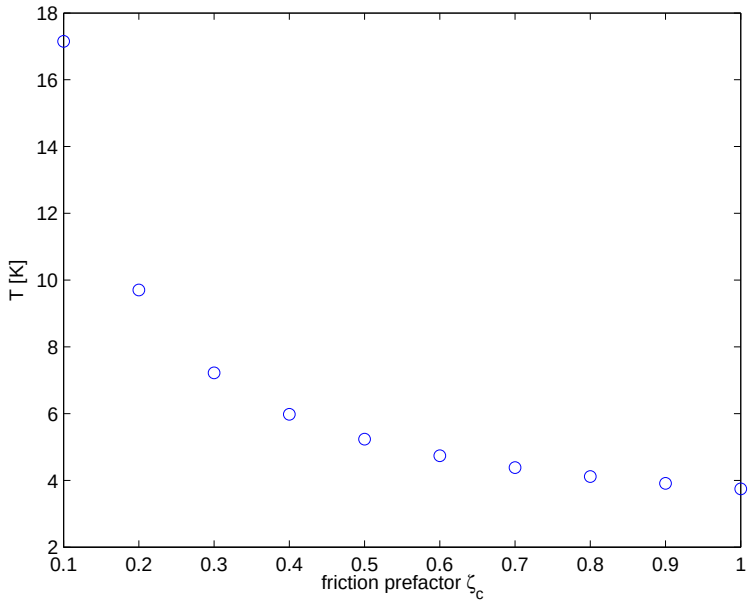

Fig. 4: Thermal equilibrium violated for the reduced coupling in the fluctuating fluid. Absence of particle fluctuations in the coupling now causes excessive energy dissipation and the particle cools down. The temperature was computed from the mean square velocity using the equipartition theorem, $k_b T = m \langle v^2 \rangle / 3$.

random forces were neglected (i.e. in the Langevin equation, unsteady Stokes equation and force coupling). Particles were assigned unit velocity and the simulation was run for 1000 time steps with $\Delta\hat{t} = 10^{-5}$ (scaled by the viscous time $L^2\rho/\eta$) and $\zeta_c = \{0.1, 0.5\}$. The algebraic and exponential decay of VAF were recovered with and without force coupling, respectively, as shown in Fig. 3. The tail is sensitive to the proximity to the nearest wall. We positioned the particle 20 diameters away from the wall; for times $t > 0.1$ ms, we observed a faster decay due to the presence of no-slip boundaries.

In the second, stochastic case, thermal fluctuations in the fluid were included through the LLNS equation. We varied ζ_c between 0.1 and 1 and collected the averages over 100 realizations. Recovery of the long-time tail is now difficult, though, because of the presence of noise. Instead, we tested for thermal equilibrium. From Fig. 4, we see that the reduced coupling violates the fluctuation-dissipation theorem, as manifested by the temperature dependence of the friction prefactor ζ_c. By contrast, with the full coupling we obtain constant temperature $T = 297.29$ K over the entire range of ζ_c, i.e. the error in temperature is now 0.2%.

3.4 Bulk relaxation time

We first consider relaxation of the chain in the bulk solution[1] from a stretched conformation into a coil, a process driven by the minimization of Helmholtz free energy. The λ-phage DNA is initially placed in a zig-zag conformation with the bonds stretched to about 75% of the maximum extension q_0. The only active non-hydrodynamic force is the Marko-Siggia spring force; hydrodynamic interactions are ignored for now. The simulation is run with $\Delta t = 10^{-5}$ s for 1 s, which is on the order of the Rouse relaxation time. We extract the actual relaxation time of the polymer by fitting an exponential to the time evolution of the directional chain stretch $\bar{X} = \max(\mathbf{r}_{i,x}) - \min(\mathbf{r}_{i,x})$, where $\mathbf{r}_{i,x}$ is the position vector of the i^{th} bead in the direction of the original stretch. As Fig. 5 demonstrates, the relaxation time τ_r for the benchmark chain with 10 springs is approx. 0.2 s. We can obtain a theoretical estimate from the Fox-Flory equation, which

[1]If a lattice field, such velocity or pressure disturbances due to HIs, needs to be included for bulk simulations (Sec. 3.4 and 3.5), the boundaries of the underlying finite-difference grid are placed sufficiently far away from the polymer, with the distance being $O(10\, S_s)$, to mimic bulk behavior.

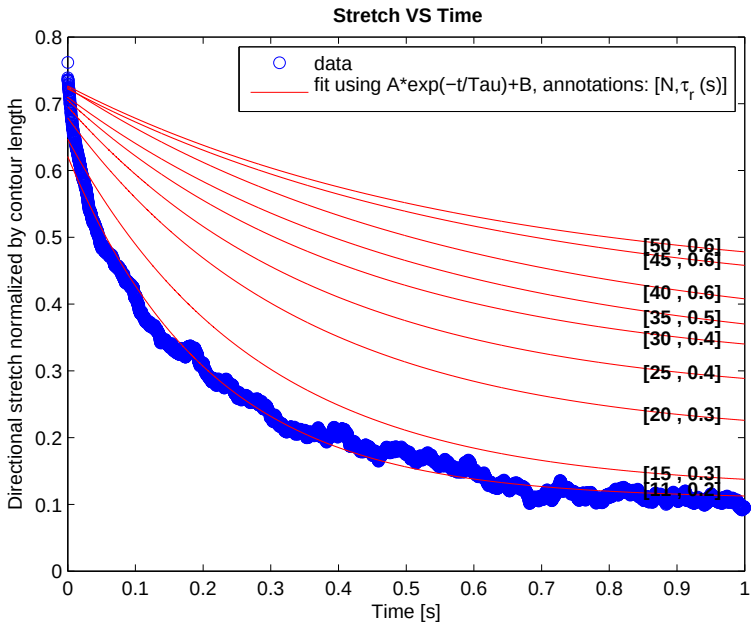

Fig. 5: Relaxation of the chain in terms of the exponential decay of directional stretch in time. The chain length (number of beads) and the relaxation time (in seconds) are given for each curve in brackets.

relates the zero shear-rate intrinsic viscosity $[\eta]$ to the molecular weight M [40],

$$[\eta] = \Phi \left\langle R^2 \right\rangle_0^{3/2} M^{-1}, \tag{44}$$

where Φ is the experimentally determined Fox-Flory parameter ($\Phi \sim 2.5 \times 10^{23}$ for a θ-solvent) and $\left\langle R^2 \right\rangle_0 = L\, b_k$ is the equilibrium mean-square end-to-end distance of an ideal chain. The Eq. (44) gives the longest relaxation time τ_r [40],

$$\tau_r = \frac{\Phi \left\langle R^2 \right\rangle_0^{3/2} \eta}{S_r R T}, \tag{45}$$

where R is the gas constant and the ratio of the characteristic to the longest relaxation time is $S_r = 1.645$ for Rouse model [40]. Eq. (45) gives $\tau_r = 0.2\,\mathrm{s}$, which compares favorably with our result. We can also use Rouse model to estimate the effective bead friction coefficient ζ from the relaxation time. Noting that polymer friction is then $\zeta_{coil} = \zeta N$, one obtains [40]

$$\zeta_{eff} = \frac{\tau_r 6\pi^2 k_b T}{\left\langle R^2 \right\rangle_0 N}. \tag{46}$$

Upon normalizing by Stokes friction ζ, we estimate the bead drag coefficient at $\hat{\zeta}_{eff} = 0.87$.

Fig. 6 shows a trajectory deviation from the free-draining model for the central bead and randomly selected realization when HIs are included through the mechanism described in 2.10. The trajectories of a free-draining model exhibit differences on the order of nanometers over the trajectories that result from a model with HIs. The significance of HIs for the benchmark chain can also be gleaned from the value of the hydrodynamic interaction parameter [40], $h^* \equiv \sqrt{3/\pi} a / R_s = 0.17$, with the typical range of $h^* \in [0, 0.5]$.

3.5 Bulk scaling laws

Next, we investigate the scaling of the radius of gyration R_g, end-to-end distance R_e and polymer diffusion coefficient D with the number of beads. The initial polymer conformation is grown on a 3-D lattice as a

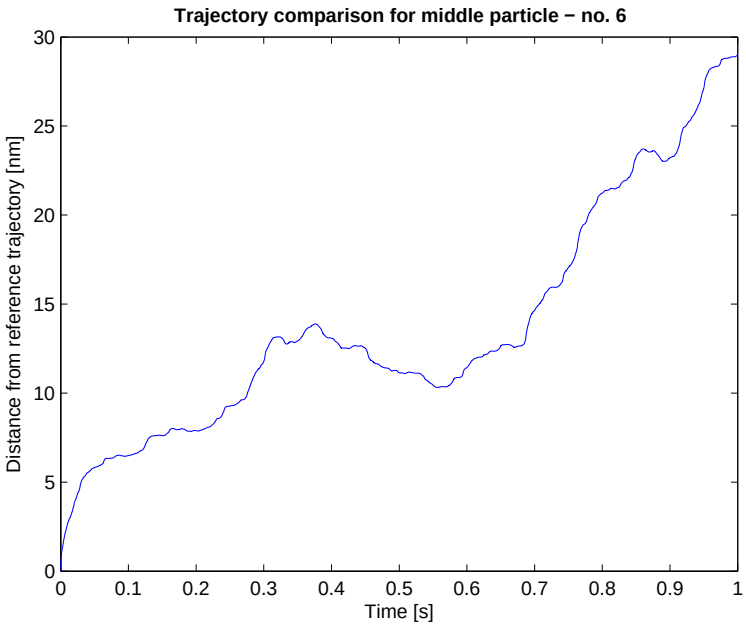

Fig. 6: The distance between trajectories of a freely-draining and hydrodynamically-interacting beads over the course of several Rouse relaxation times is on the order of nanometers.

	Polymer property		
Method	$\hat{D}$	$\hat{R}_G$	$\hat{R}_E$
Simulation	0.08	0.27	0.63
Theory	0.09	0.27	0.65

Table 1: Comparison of simulation and theoretical polymer properties for the benchmark chain $N_s = 10$

self-avoiding random walk with the equilibrium bond length of 1 micron, i.e. slightly larger than RMS bond extension R_s. The chain is then allowed to equilibrate during the first 20% of the runtime.

Fig. 7 and 8 demonstrate agreement of the scaling of the R_g and R_e obtained from the free-draining simulation with the theoretical predictions. The radius of gyration, normalized by q_0, is $\hat{R}_G = 0.27$ from the simulation, which is within 2% of the value given by the theory for ideal, Gaussian chains; [40] gives an experimental value $\hat{R}_G = 0.36$. The discrepancy between simulation and experimental data is presumably due to non-ideality of the real chains, manifested chiefly by excluded-volume interactions and HIs. To quantify this effect, we note that the hydrodynamic radius of the chain can be determined from the diffusion coefficient, $R_h = k_bT/6\pi\eta D$, which gives the ratio $R_h/R_g = 1.6$; a full HI simulation yields $R_h/R_g = 0.6$ [34].

The diffusion coefficient was computed from the Einstein formula using the mean square displacement of the center of mass of the polymer. Fig. 9 recovers Rouse and Zimm scaling of the diffusion coefficient for freely-draining and hydrodynamically coupled beads, respectively.

The agreement between theory and simulation is seen to be quite satisfactory, with the results for the benchmark chain summarized in Table 1.

3.6 Confinement simulations

To examine the effects of simple confinement on the dynamics, the chain, stretched into a zig-zag conformation, was placed into a horizontal square cross-section channel with diameters varying from 1 to 10 microns. Wall force was applied according to Eq. (11) with strength $A_w = 25k_bT$ and exclusion layer thickness

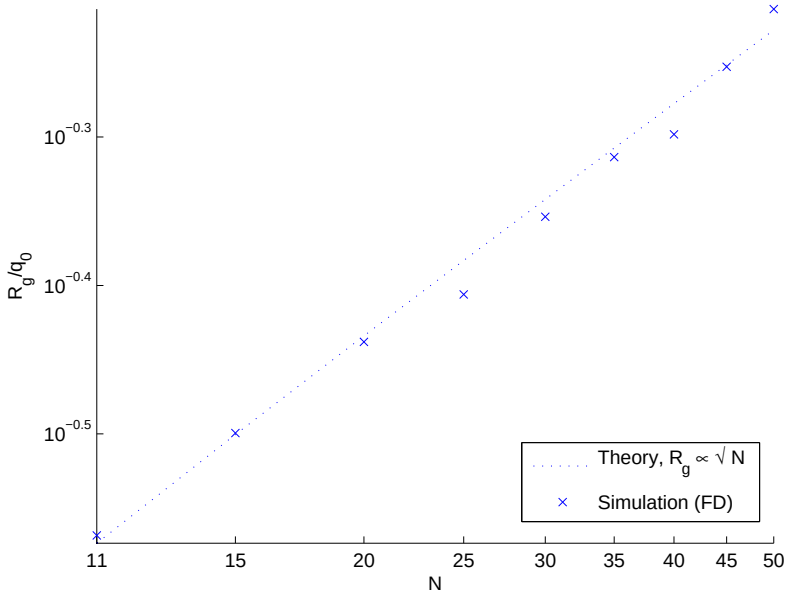

Fig. 7: Radius of gyration vs number of beads. The radius is normalized by the maximum bond length q_0.

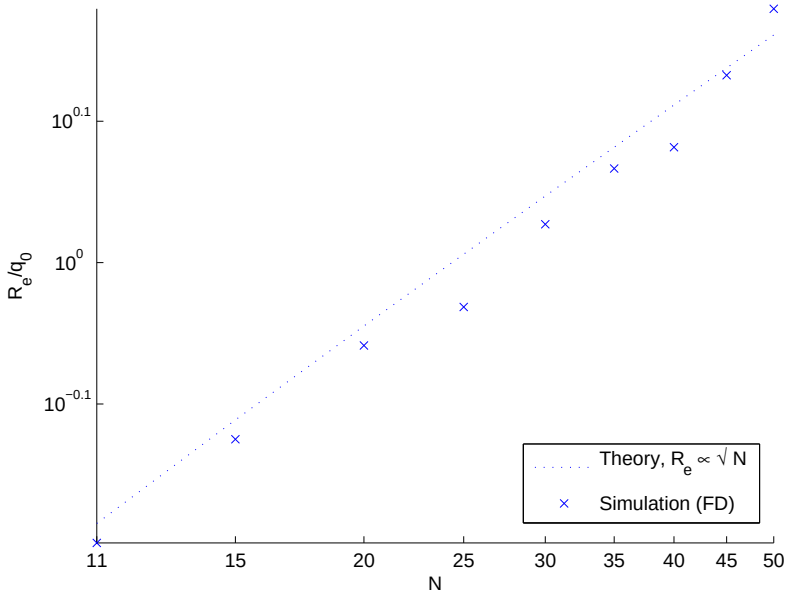

Fig. 8: End to end distance vs number of beads. The distance is normalized by the maximum bond length q_0.

$\delta_w = R_s/2$. Fig. 10 shows the free-draining dependence of the center-of-mass diffusion coefficient D on the channel diameter H. Compared to the axial diffusivity along the channel direction which transitions into a power-law scaling $D^{\parallel} \propto (1/H)^{-2/3}$ at $R_g/H \sim 0.3$ [33, 22], the three-dimensional diffusivity depicted in Fig. 10 exhibits much sharper decline with the increasing confinement and much earlier transition from the bulk value. Such behavior can be expected due to the pronounced impact of the steric wall repulsion on the mean square displacement in the direction perpendicular to the walls. The momentum imparted to the fluid

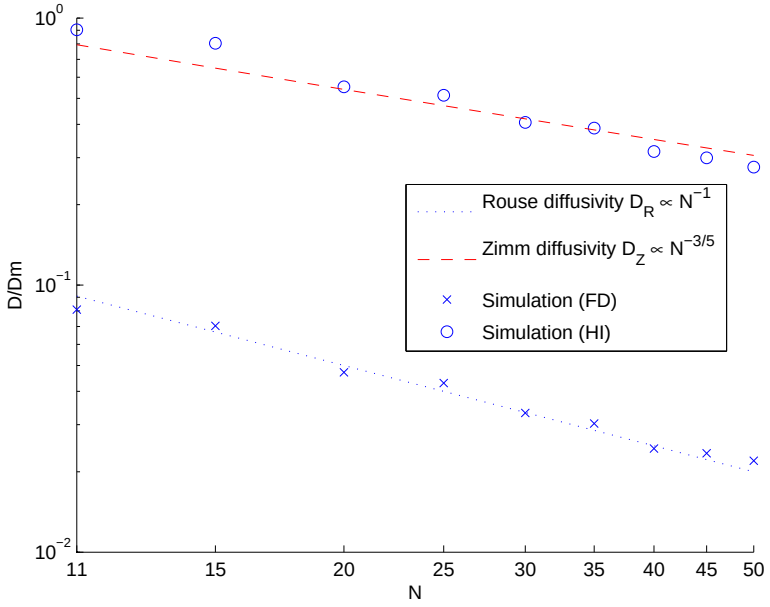

Fig. 9: Center of mass diffusivity vs number of beads, comparison of free-draining (FD) and non-draining (HI) simulations with theoretical models of Rouse and Zimm. The diffusivities are normalized by the Stokes-Einstein diffusion coefficient. Zimm scaling exponent 3/5 is based on the Flory approximation [65, 58].

by the localized beads is, in large part, absorbed by the no-slip boundary condition on the stationary walls, which justifies the use of free-draining simulations for the prediction of diffusivity data. The wall repulsion creates a steric boundary depletion layer, as confirmed by a unimodal probability distribution function of the chain center-of-mass in Fig. 11. The maximum is centered around the channel centerline and the variance is inversely proportional to the thickness of the depletion layer and the degree of confinement.

Since the confinement increases viscous drag on the chain, and the zero-shear viscosity is proportional to the relaxation time ($\mu_0 \sim G\tau$, where G is the characteristic modulus), the relaxation time increases accordingly. We note in conclusion that confinement may produce other, more subtle, effects, not addressed in this work; one such area of active research is the alteration of entropic force laws due to the loss of chain configurational space. It has been shown [74] that the correction is prominent very close to the walls and scales as $1/N$.

4 Polymer translocation in entropic traps

In Sec. 4.1-4.2 we apply the developed model to the molecular-weight-based separation of DNA using entropic barriers. After reviewing the basic theory in Sec. 4.1, we observe the limiting cases of trapping and flowing regimes, identify the transition region between the two by inspecting the character of the mobility curve and confirm the validity of the kinetic models recently reported in the literature in Sec. 4.2.

4.1 Theoretical background

Traditional DNA separation by electrophoresis is problematic for long chains. In free-solution, the electrophoretic mobility μ ($\mu \equiv \langle v \rangle / E_{av}$, where $\langle v \rangle$ is the mean axial center-of-mass velocity and E_{av} is the magnitude of the external electric field strength) is independent of the length of a polyelectrolyte (or, equivalently, molecular weight) after a certain threshold length. Recent multiparticle-collision dynamics [20] and molecular dynamics (MD) [23] studies suggest that for very short chains (typically 50 monomers or less) of synthetic polymers and single-stranded DNA (ssDNA), the mobility exhibits a maximum; no such maximum

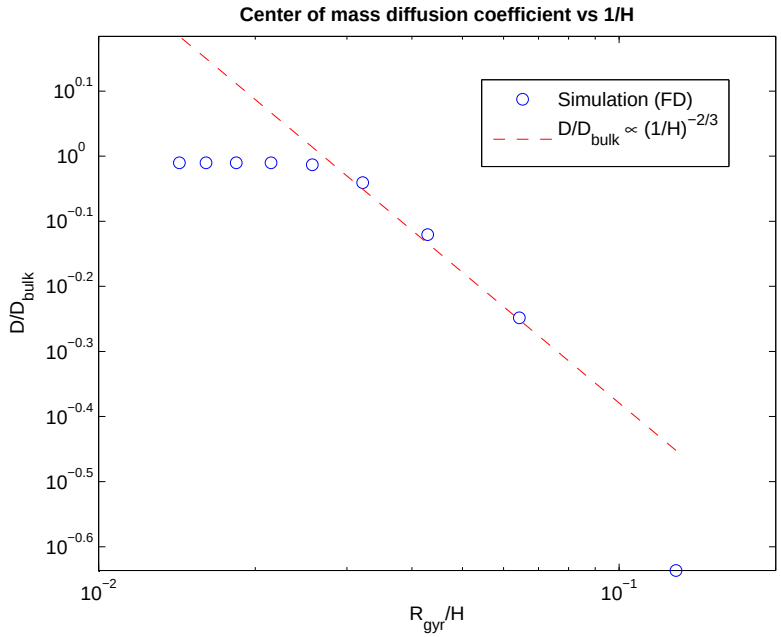

Fig. 10: The 3D center-of-mass diffusion coefficient (normalized by its bulk value) shows an earlier and steeper decline with the increasing confinement (normalized by the equilibrium radius of gyration) compared to the 1D axial diffusivity which scales as $D^{\parallel} \propto (1/H)^{-2/3}$ (dashed line, shifted to overlap with the data set for reference).

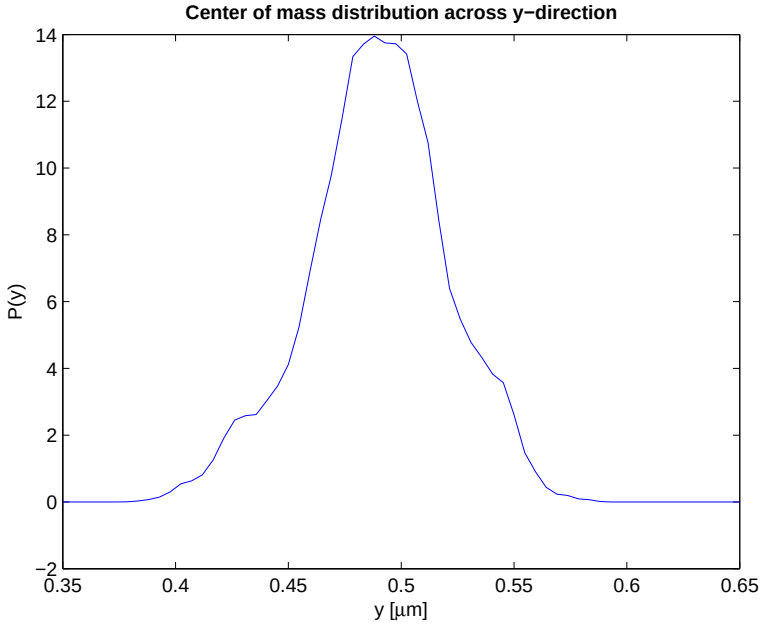

Fig. 11: The probability distribution function of the chain center-of-mass across channel cross-section in strong confinement ($H = 1$ micron). Histogram created using a Gaussian kernel density estimator of Botev [12].

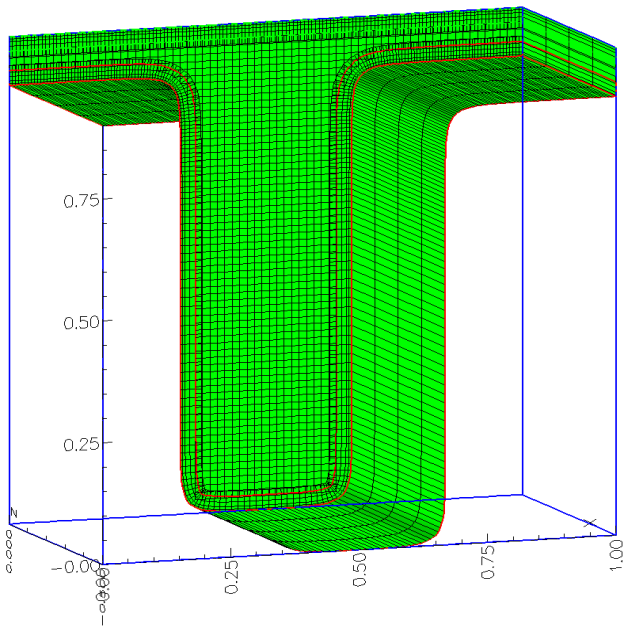

Fig. 12: Meshed entropic trap geometry with overlapping, mutually interpolating grids. In the simulation we use an array of four traps in a series. The lengths are scaled by h_l.

was found for double-stranded DNA (dsDNA). In gel electrophoresis, μ is inversly proportional to chain length, making separation of long chains inefficient.

One of the methods to increase separation efficiency is to use an "artificial gel", such as a spatially periodic geometry consisting of a series of alternating thin and thick regions, known as entropic traps [27], see Fig. 12. In the prevalent configuration, the depth of the thick region h_l is of the order of R_g, while the thin region is shallower, $h_s < R_g$. The driving force behind translocation can be an electric field or pressure-driven flow. In standard experimental protocols, the DNA is dissolved in a buffer, labeled with a fluorescent dye and observed under an optical microscope and/or tracked with a CCD camera [6].

Under proper conditions, long molecules will travel faster than the short ones. Such a seemingly counter-intuitive observation can be explained by a simple kinetic model proposed by Han [27], which assumes, in analogy with the transition state theory, an Arrhenius form for the trapping time,

$$\tau_{trap} \sim \tau_0 \exp(\Delta F), \tag{47}$$

where ΔF is a free energy difference between the trapped state and the activated state (where the chain is partially inserted in the shallow region) and τ_0 is the activation time. The two contributions to the free energy difference are the potential energy gain due to electric field and conformational entropy loss due to confinement in the shallow region. Adopting the blob model for polymers, we can express $\Delta F \sim m - m^2 E_s$, where m is the number of blobs inserted in the shallow region and E_s the electric field strength in the shallow region. Wong [73] presents a more detailed model with

$$\Delta F = \frac{m}{D^{1/\nu}} - \frac{Q E_s m^2}{c\, D^{1/\nu - 1}}, \tag{48}$$

where D is blob diameter, Q the net charge of the inserted segment, ν the polymer size exponent (0.59 for ideal chains) and the constant c equals 2 and 4, respectively, for linear and hairpin conformations. In a hairpin conformation, the polymer is folded on itself with both ends in the (same) deep region while another section of the chain is partially inserted in the shallow region. The authors also propose that the higher mobility (or shorter translocation time) of long chains can be linked to the prevalence of hairpin translocations; linear, single-file translocations, on the other hand, are favored by short chains. Since τ_0 is proportional to the contact area between the shallow region and the chain, we have $\tau_0 \sim N^{-\nu} D^{-1}$.

It has been shown [55] that the dynamics of translocation across a series of traps is governed by more than one time scale; this, in fact, leads to a non-monotonic dependence of the mobility on the chain length. We can split the translocation time τ into the approach time τ_{app}, activation time τ_{act} and transit time τ_{tran}, $\tau = \tau_{app} + \tau_{act} + \tau_{tran}$, which characterize, respectively, the diffusion within the spacious cavity and the approach to the transition region, overcoming of the entropic barrier and partial penetration into the slit and, finally, electrophoretic migration through the slit. The trapping time is then $\tau_{trap} = \tau_{app} + \tau_{act}$.

Fig. 13 gives a qualitative picture of how the relative magnitudes of these time scales determine the location of the maximum in μ. Apparently, two limiting types of behavior can be observed, depending on the electric field strength and the geometric ratio h_s/h_l: mobility increasing with N, characteristic of entropic constrictions [27], and mobility decreasing with N, characteristic of nanopores [37].

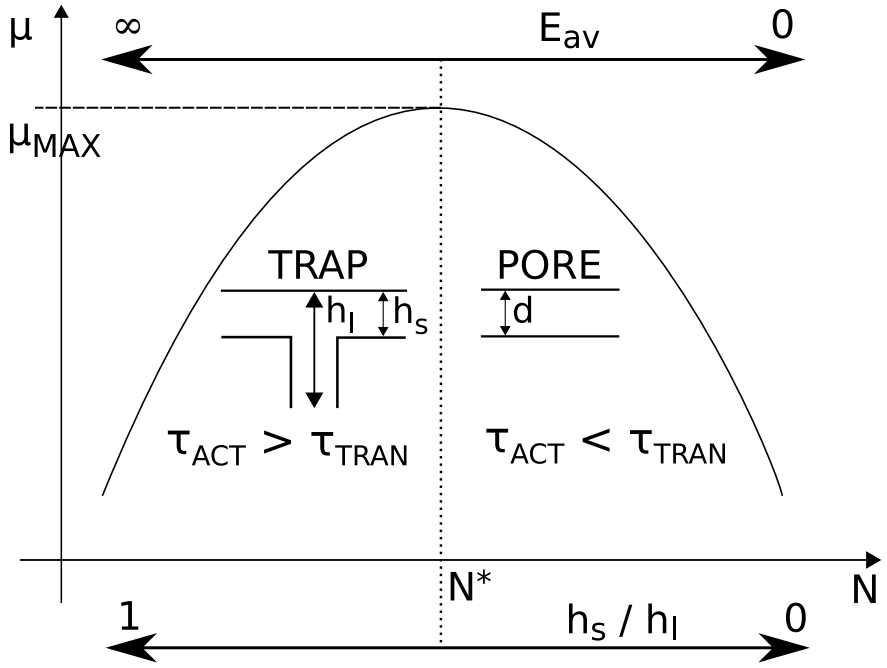

Fig. 13: Non-monotonic dependence of electrophoretic mobility on chain length. The crossover value N^*, corresponding to the maximum in mobility, shifts to the left with the increasing average electric field strength, E_{AV} and/or with increasing h_s/h_l ratio. This reduces the activation barrier and enhances transit through the shallow region, thus $\tau_{act} < \tau_{tran}$, making the transit time the dominant time scale determining the overall dynamics. The 'pore' region expands at the expense of the 'trap' region and the mobility decreases with N throughout most of its range. Similar arguments apply to the shift in the opposite direction.

4.2 Simulation results

The dimensions of one trap (see Fig. 12), scaled by the height $h_l = 3\,\mu$m, are: length $L_t = 1$, width $W_t = 0.5$ and height and length ratios of shallow to deep region, respectively, $h_s/h_l = 0.1$, $l_s/l_l = 2$. These ratios are both twice as large as those used in the original geometry proposed in [27]. The motivation for such increase is to reduce the entropic barrier, thus increasing chain mobility and reducing computational time; the disadvantage, however, is the reduced trapping time at the expense of transit time, which results in decreased selectivity of separation, defined in [26] as $S \equiv \frac{d\mu}{dN} = \frac{\mu_0}{N} \frac{\tau_{trap}/\tau_{tran}}{(1+\tau_{trap}/\tau_{tran})^2}$, where μ_0 is the free-space mobility. We use four traps in a series with the electric field varied in the physiological range between 10 and 160 V/cm and the number of beads N varied between 11 and 76. The simulation is run for 10^5 timesteps or until the center-of-mass exits the geometry, whichever occurs first, with the time step $\Delta t = 10^{-5}$ s and 50 realizations. We neglect hydrodynamic and electrostatic interactions between the beads (Debye screening length κ^{-1} in typical buffers of ~ 50 mM concentration is of the order of nanometers) and electro-osmotic flow (suppressed due to wall coating).

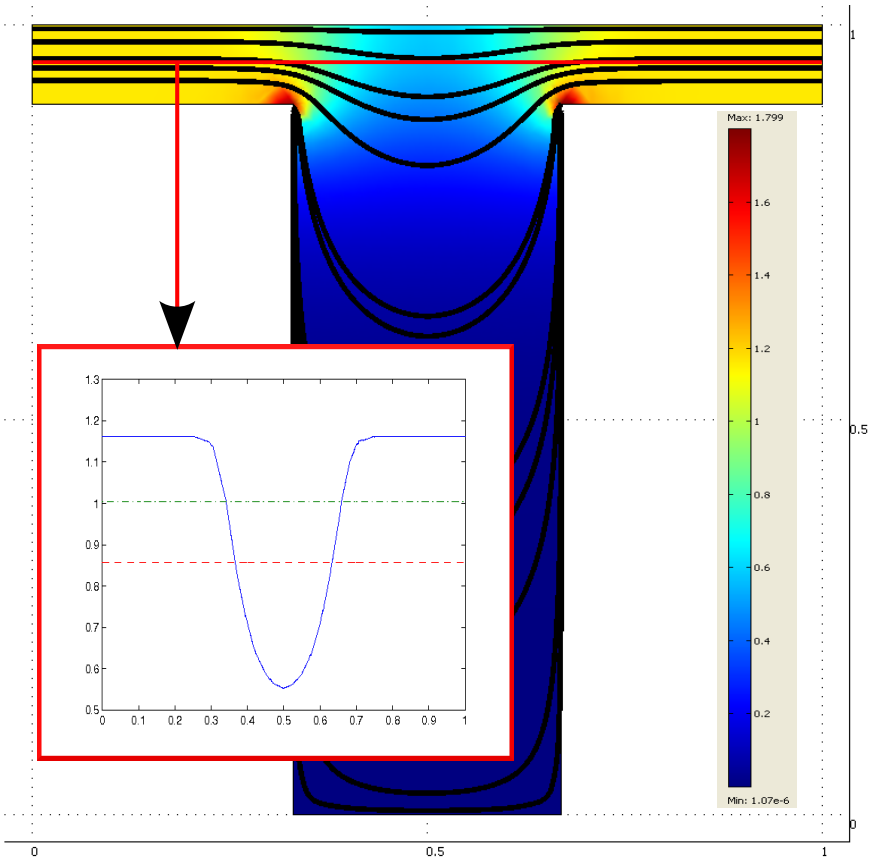

Fig. 14: Electric field lines in the trap. Inset: Solid line – normalized electric field strength along the midline of the narrow region; dash dotted line – integral average $E_{AV,1} = 1$, dashed line – arithmetic average $E_{AV,2} = 0.86$.

We note that for $l_s/l_l \neq 1$, the integral average of electric field strength, $E_{AV,1} \equiv 1/L_t \int_0^{L_t} E(x)dx$ will differ significantly from the commonly employed arithmetic average of electric fields in shallow and deep region, $E_{AV,2}$. The comparison of these two averages, along with the electric field lines and the variation of the magnitude of the electric field strength along the midline of the narrow region, is depicted in Fig. 14.

The charges in a polyelectrolyte are screened due to counter-ion condensation; the screening factor $\alpha \equiv Q_{eff}/Q$, where Q_{eff} is the effective charge, can be calculated for infinite dilution from the Manning prediction, $\alpha = b_c/l_b$, where $b_c = 1.7$ Å is the charge spacing in DNA and $l_b = 7.1$ Å is the Bjerrum length for water. This yields $\alpha = 24\%$, which is within the range given in literature [19]. Such an estimate should, however, be only interpreted as an upper bound, since single-molecule studies of DNA are typically carried out in solutions with electrolyte concentration > 10 mM, where the large number of counterions adsorbed along the chain backbone is sufficient to make the DNA chain effectively uncharged, decreasing its persistence length and increasing flexibility [63]. Assuming the experimental free-draining mobility of a DNA chain in a 40 mM tris-acetate buffer to be $\mu_0 = 3.0 \times 10^{-8}\mathrm{m^2 s^{-1} V^{-1}}$ [67] and adopting the Rouse model with chain friction $\zeta_{chain} = N\zeta$, we estimate the effective charge per bead as

$$Q_{eff} = \mu_0 6\pi\eta a = 270\ e, \tag{49}$$

where e is the electron charge. Alternatively, we can use

$$Q_{eff} = \frac{N_{bp}}{N} \times Q_{bp} \times \alpha, \tag{50}$$

where the charge per base pair Q_{bp} is $2e$ and the number of base pairs N_{bp} is calculated from the contour length L as $N_{bp} = \frac{L}{R_{bp}} \simeq 62$ kbp, where the rise-per-base-pair $R_{bp} = 3.4$Å. Consistency between

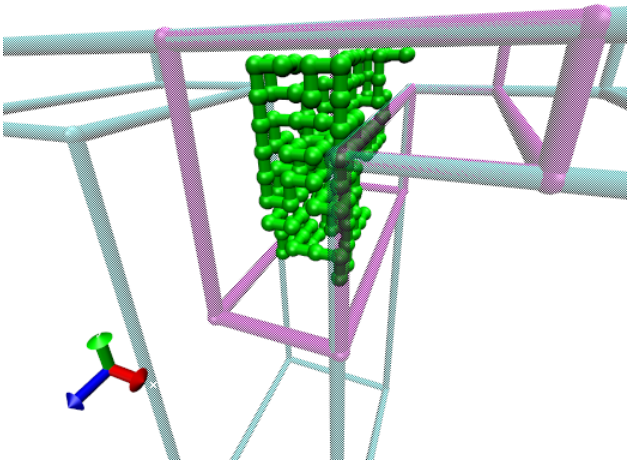

Fig. 15: Bounding polyhedron with the chain of 100 beads in the initial configuration after a bounded, three-dimensional random walk on a discrete lattice.

Eqs. (49) and (50) is achieved with screening $\alpha = 2.5\%$. More rigorous estimates of Q_{eff} can be obtained from molecular dynamics simulations after explicit introduction of counterions into the solution to guarantee electroneutrality, as was done for short polyelectrolytes in [24].

To further reduce the activation time τ_{app} and thus the overall computational time, we preposition the chain in the transition region, at the interface between a thick and thin region (Fig. 15). The initial conformation of the chain is grown on a lattice as a bounded, self-avoiding random walk. To make sure the chain remains within the bounding polyhedron during the walk, a point-in-polyhedron and point-in-polygon problems needs to be solved repeatedly at each step. This is done by a ray-crossing test, based on the Jordan curve theorem: we run a semi-infinite ray from the query point and count how many faces it crosses; odd and even number of crossings correspond, respectively, to the query point being inside and outside the bounding volume.

Fig. 16 shows the mobility of the chain with respect to the external electric field, $E_{av} = \Delta V/L$, with the applied voltage ΔV ranging from 0.01 to 0.2 V and N from 11 to 41. The mobility in the channel can be related to the free-space mobility, μ_0, as

$$\frac{\mu}{\mu_0} = \frac{\tau_{tran}}{\tau_{tran} + \tau_{trap}}, \tag{51}$$

where $\tau_{tran} = L/\mu_0 E_{av}$ [27]. Since $\tau_{trap} = 0$ for electrophoresis in a regular channel, we obtain μ_0 from the plateau region of Fig. 16, $\mu_0 = 2.36 \times 10^{-8} \mathrm{m^2 s^{-1} V^{-1}}$. We can then calculate the trapping time from Eq. (51),

$$\tau_{trap} = \frac{L}{E_{av}} \left(\frac{1}{\mu} - \frac{1}{\mu_0} \right), \tag{52}$$

depicted in Fig. 17. The semi-logarithmic curve dependence of $\ln(\tau_{trap})$ on $1/E_{av}$ can be fitted with a linear function, whose slope A and y-intercept B can then be used to fit the mobility curve in Fig. 16 with an exponential, derived from Eqs. (47) and (51), after recognizing that $\Delta F = A/E_{av}$,

$$\mu = \frac{\mu_0}{1 + C E_{av} \exp \frac{A}{E_{av}}}, \tag{53}$$

where $B = \ln(\tau_0)$ and $C = \mu_0 \exp(B)/L$.

4.3 Conclusions

We observe that the two characteristic behaviors of the chain mobility in Fig. 18, one for $E = 8.3$ V/cm and the other for $E = 25$ V/cm, are in agreement with the qualitative schematic described in Fig. 13. While the

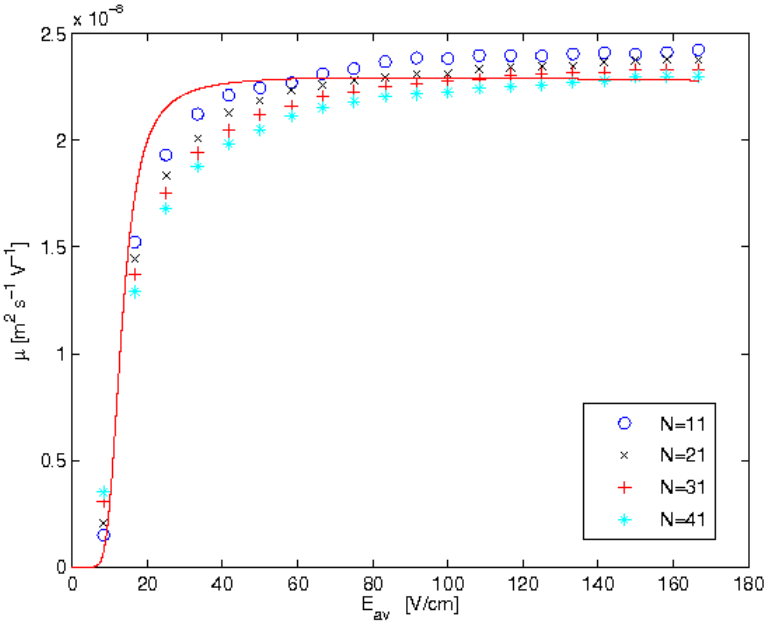

Fig. 16: Electrophoretic mobility, calculated as $\mu = \langle v \rangle / E_{av}$, vs average electric field strength. Exponential fit of the mobility curve uses the slope and intercept of the linear fit of the trapping time curve, Fig. 17.

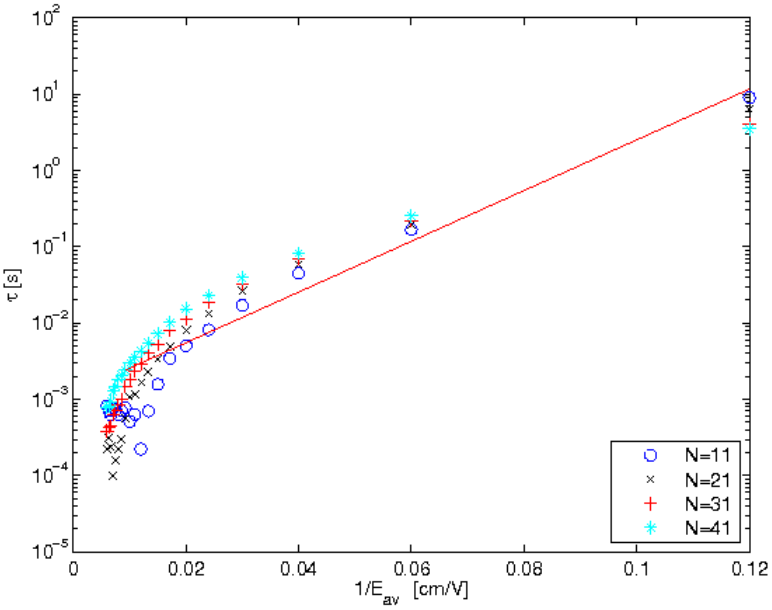

Fig. 17: Trapping time vs average electric field with a linear fit. For $E > 50$ V/cm, τ_{trap} is small (compared to τ_{trans}); such data were thus discarded from the fit.

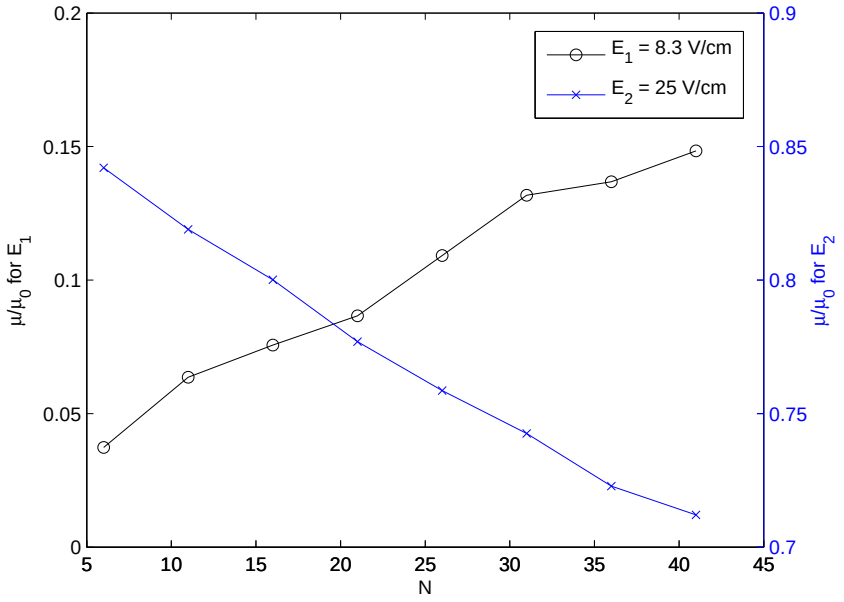

Fig. 18: Electrophoretic mobility vs chain length. For $E = 8.3$ V/cm, trapping regime dominates; for $E = 25$ V/cm, electrophoretic migration dominates.

mobility μ increasing with chain length is typical of entropic traps and suggests τ_{act} as the dominant time scale, the decreasing dependence of the mobility μ on chain length identifies τ_{trans} as the dominant time scale, typical of channel translocation. To further quantify the behavior sketched in Fig. 13, we find that the maximum in the mobility curve occurs for $E \sim 12$ V/cm, seen in Fig. 19.

The simulations also corroborate the validity of the kinetic model presented in Sec. 4.1. Fig. 20 shows snapshots of short (N=11) and long (N=41) chains at different times during simulation. The long chain can expose more beads to the transition region between the deep and shallow cavities than the short chain and is thus more likely to migrate under the influence of the electric field.

The true free-space mobility μ_0 was also determined from the simulation in a cylindrical channel, yielding a value of $(2.98 \pm 0.006) \times 10^{-8} \mathrm{m^2 s^{-1} V^{-1}}$. This value naturally agrees with our starting value used in Eq. (49) and is within 20% of the apparent plateau mobility obtained from the entropic trap array. While the average electric fields in the channel and the trap are the same (cf. Fig. 14), the vanishingly small electric field in the deep region cannot compete with thermal diffusion ($\sim k_b T/a$), which is the most likely reason for the discrepancy between the two free-space mobilities. We note that an approximate formula based purely on geometrical dimensions of the domain and employed in [68] gives the ratio of the true and apparent free-space mobilities as 2.8, suggesting an even larger discrepancy.

5 Polymer translocation in nanopores

The study of translocation times of polymer transport across a nanoporous membrane is another suitable candidate for the application of the hybrid model developed above.

Analytically, the translocation process can be described as diffusion over a free energy barrier [52]. For a Gaussian chain, the heat equation, with the time variable replaced by the number of Kuhn segments, governs the probability distribution of the chain conformation. Given the knowledge of the specific geometry of the translocation domain (e.g. a cylindrical pore, parallel plates or spherical cavities), pore-polymer interactions and applied gradient in electrochemical potential that drives the translocation, this equation can be solved and the entropy and free energy of confinement can be computed from the probability distribution using standard methods of statistical thermodynamics. The free energy landscape, in turn, determines the drift in

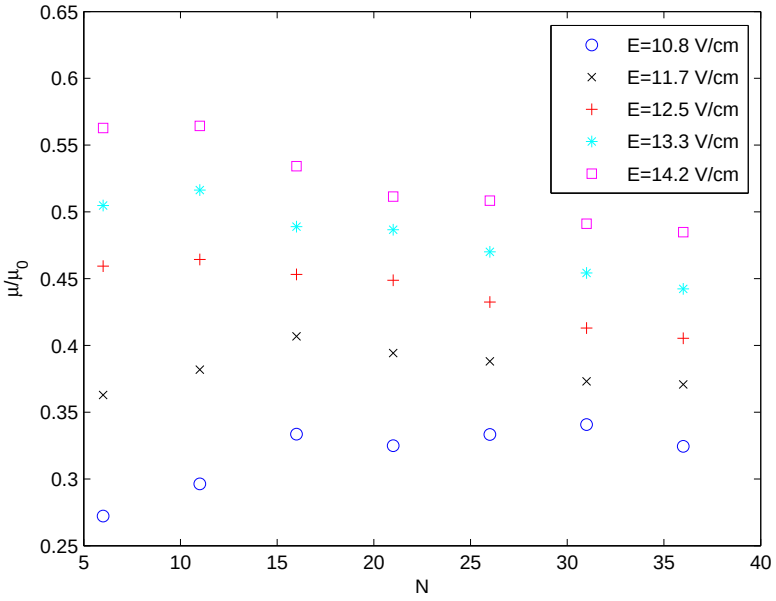

Fig. 19: Change in the monotonicity of the curve suggests transition from the free flowing behavior to the trapping behavior. The maximum occurs for $E \sim 12$ V/cm.

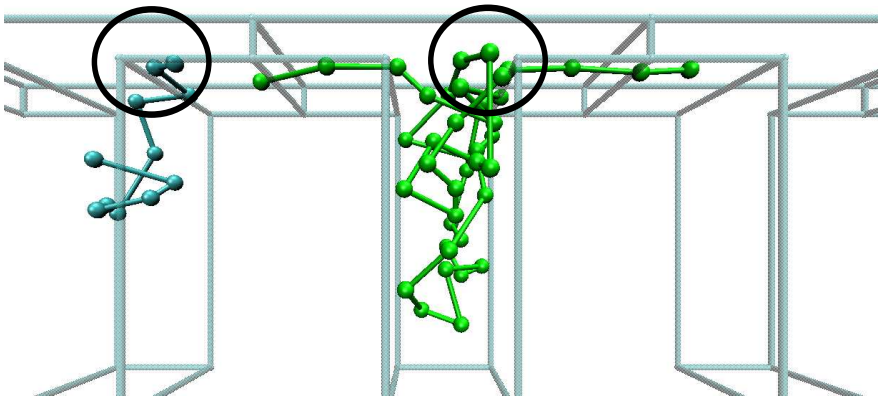

Fig. 20: Snapshots of short (N=11) and long (N=41) chains at time t=0.5s (left) and t=1s (right). Left: Long chain has more beads facing the slit than the short chain and thus higher probability of transit (activation regions circled). Right: While the long chain successfully migrated into the middle trap and nucleated into the next shallow region, the short chain is delayed in the activation stage negotiating the free energy barrier.

the Fokker-Planck equation governing the transition probability of a Markov process. Solving this equation subject to absorbing boundaries (corresponding to successful translocation events) yields the transition probability, which in turn can be related to the probability distribution function of the first-passage times (FPT) and its first moment, the average translocation time [43]. The probability distribution function of the FPT is skewed – it rises sharply to a maximum and then decreases roughly algebraically. As expected, it is also compressed to shorter times for higher translocation velocities (or, equivalently, stronger driving forces). The translocation can, however, only take place after the free energy maximum has been crossed, i.e. a sufficient number of monomers has been inserted into the channel. In some experimental setups, such as entropic traps (Sec. 4.1), this activation process can be a rate-determining step; the nucleation theory of phase transitions then provides a qualitatively reasonable description. Once the nucleation barrier is surmounted, the average translocation time $\langle t_D \rangle$ is found to be proportional to the chain length and inversly proportional to the driving force $\Delta\mu$ (such as voltage difference ΔV applied across the pore),

$$\langle t_D \rangle \propto \frac{N}{\Delta\mu}. \tag{54}$$

The assumption of quasi-equilibrium implicit in the translocation theory can be violated for chains of large molecular weights, whose relaxation times exceed those of translocation. The simulations of uncharged chains in non-equilibrium conditions suggest $\langle t_D \rangle \propto N^\alpha$, $\alpha > 1$, where different values of the size exponent α have been proposed in the literature depending on the experimental conditions (see [52] for summary).

Computationally, the translocation is typically addressed using molecular dynamics [3, 47] or Monte Carlo simulations [44]. When the interest is in the translocation phase only (rather than capturing and/or activation), then the chain is typically pre-positioned into a confined region of radius equal to the free solution radius of gyration of the chain [19], or the terminal bead tethered to the pore entrance during equilibration [70, 32]. We follow the latter approach of bead tethering. Experiments and theory (assuming Arrhenius form of the activation time) suggest that the activation time decreases with chain length for long chains (due to prevalence of hairpins) and increases with chain length for short chains (due to single-file conformations) [73]. The effects of hairpins on translocation time t_D have been found to be due to the following phenomena: 1) more strands with more beads in the pore result in larger electrostatic force (t_D decreases); 2) folded hairpin effectively shortens the chain length (t_D decreases); 3) hairpins increase frequency of bead-bead and bead-wall collisions leading to increased friction (t_D increases). In a simulation, t_D can be determined 1) by having the chain associated with a clock that starts when the first bead enters the pore, resets when chain fluctuates back to the *cis* side (to exclude unsuccessful translocation attempts) and stops when the last bead exits the pore on the *trans* side [70], or 2) by monitoring the duration of blockades of the channel current [51, 49]. Alternatively, escape from the pore can be monitored instead of the translocation, since the escape and translocation times follow identical scaling [32].

5.1 Simulation Setup

In the following we compare two solution methodologies: a coarse-grained (CG) CLEPS [54]-like model developed in Sec. 2 with mesoscale treatment of forces and a fine-grained (CG) molecular dynamics model with the more fundamental atomistic potentials. We assume interaction between the biological membrane and polymer to be only of steric origin [69]; the surface of the pore is uncharged so as to prevent electroosmotic flow, allowing us to isolate the effects of hydrodynamic interactions. Following Matysiak [47], we take α-hemolysin protenacious pore embedded in lipid membrane as a prototypical model of a biological pore, with pore length $L = 48$ Å, pore diameter $D = 15$ Å, and with deionized water at room temperature as the solvent. The simulation was preceded by equilibration over 25 Rouse times (i.e. $2000\Delta t$, where $\Delta t = 0.1$ps), with the pore closed (artificial wall imposed at the pore entrance), electric field turned off and terminal bead tethered to the center of the pore entrance. The initial polymer conformation was a zig-zag or, alternatively, it was grown on a lattice with step size b_0 as a self-avoiding random walk (SARW) bounded by a region of the radius equal to the bulk radius of gyration of the chain. No statistically significant difference was found with sufficient equilibration. After equilibration, the tethering was released, pore opened and electric field turned on. The results were averaged over 800 realizations.

5.1.1 Coarse-grained model

The forces acting on the beads are: frictional, Brownian, wall force ($A_w = 40k_bT, \delta_w = b_k/2\sqrt{q_0/b_k} \approx 0.4L$), Marko-Siggia spring force and excluded-volume force.

The coarse-graining of the ssDNA chain (Poly(dA))is based on the following Matysiak's parameters [47]: monomer mass $m_m = 312$ amu, number of monomers (bases) $N_m \in \langle 10, 100\rangle$ and base-to-base distance (monomer diameter) $a = 4$ Å, which yields contour lengths $l = N_m a \in \langle 40, 400\rangle$ Å. Assuming $N_{ks} = 10$ Kuhn segments per spring and Kuhn length $b_k = a = 4$ Å, we obtain:

- maximum spring extension $q_0 = N_{ks} b_k = 40$ Å,
- excluded volume interaction parameter $v \propto b_k^3 = 64$ Å^3, and
- initial bond length $b_0 = b_k\sqrt{N_{ks}} = 13$ Å.

For $N_m \in \langle 10, 100\rangle$, the number of springs is $N_s = l/q_0 = N_m b_k/q_0 = N_m/N_{ks} \in \langle 1, 10\rangle$. The remaining parameters are a function of the number of beads, $N_b = N_s + 1$: bead mass, radius and charge.

- For bead mass, we have $m_b = N_{ks} N_s m_m/N_b \approx 10\, m_m = 3120$ amu.
- To obtain bead radius a_b, we assume θ-solvent and the worm-like chain being in the ideal chain limit, so that $R_g^2 = \langle R^2\rangle_0/6 = l b_k/6$. To illustrate, for $N_s = 1$, i.e. $l = N_s q_0 = 40$ Å, we calculate intrinsic viscosity $[\eta]_0 = \Phi\langle R^2\rangle_0^{3/2}/M$, where the Flory-Fox parameter $\Phi = 1.67\times 10^{23}$ [40] and molecular weight $M = N_m m_m = N_b m_b$. This yields the longest Rouse relaxation time $\tau_1 = [\eta]_0 M\eta_s/(RT\pi^2/6) = 0.08$ ns, where solvent viscosity $\eta_s = 1 \times 10^{-3}$ Pa·s. Using the Rouse model further, we get the bead drag coefficient $\zeta_b = 24k_bT\sin^2(0.5\pi/N_b)\tau_1/b_0^2 = 2.56 \times 10^{-12}$ kg/s, where the number of beads $N_b = 2$. Finally, using the Stokes expression we get bead radius $a_b = \zeta_b/(6\pi\eta_s) = 1.36$ Å.
- For bead charge, we have $Q_b = N_{ks} N_s q_m/N_b$, where the monomer charge $q_m = 0.4e$ (an optimal value obtained in [47] by fitting the translocation time dependences to experimental data). The total charge conservation and total mass conservation (see above) thus hold between both coarse-grained and fine-grained models.

5.1.2 Fine-grained model

The relevant molecular dynamics parameters are taken from Matysiak [47]. The polymer is represented by a finer-grained pearl-necklace model whose beads now represent the DNA bases as the relevant repeat units. The Marko-Siggia spring is replaced by harmonic bond and harmonic angle potentials, the excluded-volume force is replaced by the repulsive part of the Lennard-Jones potential and the wall force is replaced by the full Lennard-Jones potential. The effects of Langevin thermostat are mimicked by the Brownian dynamics forces, which include both drag and random components.

5.2 Simulation Results

In this section we report the dependences of the pore translocation times on molecular weight (which is proportional to the number of beads) and voltage differences applied across the pore. Further we compute electrophoretic mobilities both in the pore and in free solution and show the dependences on molecular weight and Peclet number ($Pe = q_m q_0 \Delta V/(Lk_bT)$).

To exclude unsuccessful translocation attempts from the statistics, the translocation time t_D is determined as in [70]: the clock associated with each chain is on whenever at least one bead is inside the pore, and is reset whenever the chain fluctuates back to the donor compartment leaving no monomers in the pore.

For the coarse-grained (CG) model, Fig. 21 shows the dependence of the translocation time on the number of beads N_b. We observe superlinear scaling for the ratio of polymer length to pore length $l/L \leq 0.12$ and linear scaling for $l/L > 0.12$, i.e. the size exponent α exhibits a marked decrease around this threshold ratio, which corresponds to $N_b = 3$. A similar trend was observed in an experiment by Meller [49], who observed translocation velocity rapidly decreasing with N_b for short chains and slowly decreasing, almost constant, for long chains. The rationale for such behavior can be found in the nucleation theory of translocation [52], which

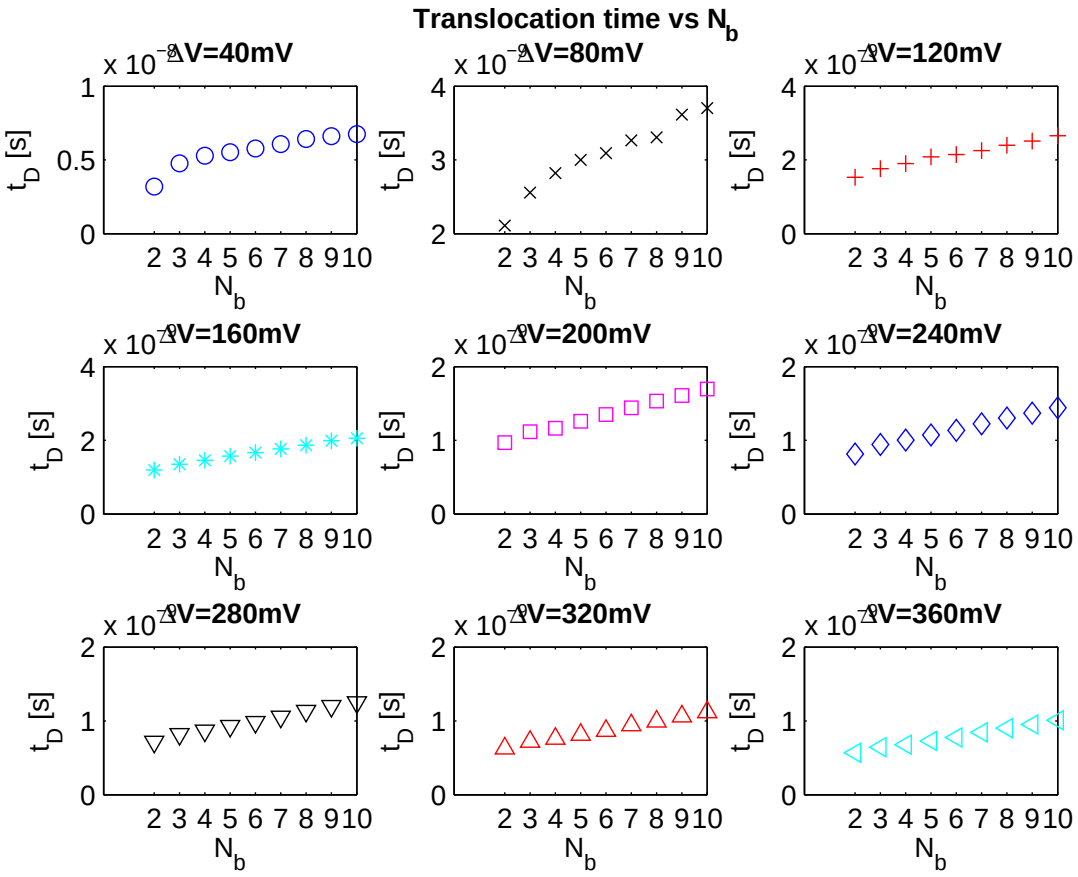

Fig. 21: Translocation time vs number of beads (CG model) showing two translocation regimes.

gives the nucleation time as the reciprocal of the nucleation rate determined from free energy arguments. The theory correlates the decrease in the size exponent with the decrease of the nucleation time. As in the entropic traps, the longer chain in a folded conformation exposes more of its contour to the pore entrance compared to a short chain, increasing the likelihood of crossing the free energy barrier and proceeding to translocation. The transition in Fig. 21 is less obvious for large voltage gradients, which is likely due to the prepositioning of the chain at the pore entrance: the energy barrier decreases with the increasing driving force, making it less likely for the chain to relapse to the donor compartment after partial insertion into the pore. The translocation time then dominates the activation time and determines the dynamics of the transport. Fig. 22 depicts the translocation time dependence on the voltage difference ΔV applied across the pore, where ΔV varies between 20 and 340 mV. By fitting the above dependences to experimental data, the choice of adjustable parameters ζ and q_m can be iteratively improved. Fig. 23 depicts the distribution of the translocation times $\psi(t_D)$, which shows an asymmetric, right-tailed distribution with positive skew, as predicted by the theory [52] and confirmed by experiments [47].

For the fine-grained (FG) model, the monomers and coarse-grained beads coincide. Fig. 24 shows the dependence of the translocation time t_D on the applied voltage difference ΔV, where ΔV varies between 100 and 340 mV. Only the linear scaling of the translocation time with N_b is now observed over the studied range of molecular weights, as expected for negligible activation time due to strong driving force. Compared to the results of the coarse-grained model, we observe increase in translocation time by a factor of 10, corresponding to a proportional increase in the friction coefficient. This leads to enhanced chain retardation in the pore, presumably due to a more realistic wall potential, which now includes van der Waals attraction, and due to the increased number of structural units interacting with the wall.

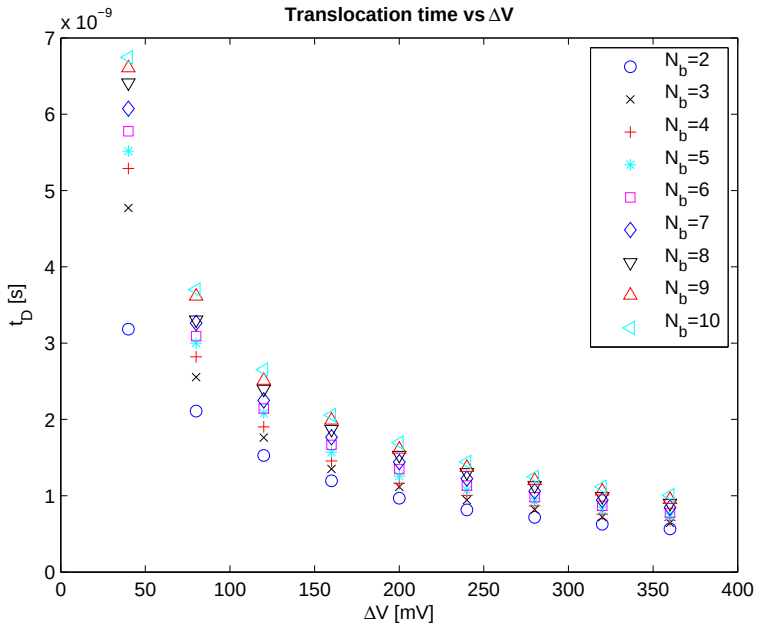

Fig. 22: Translocation time vs applied voltage (CG model).

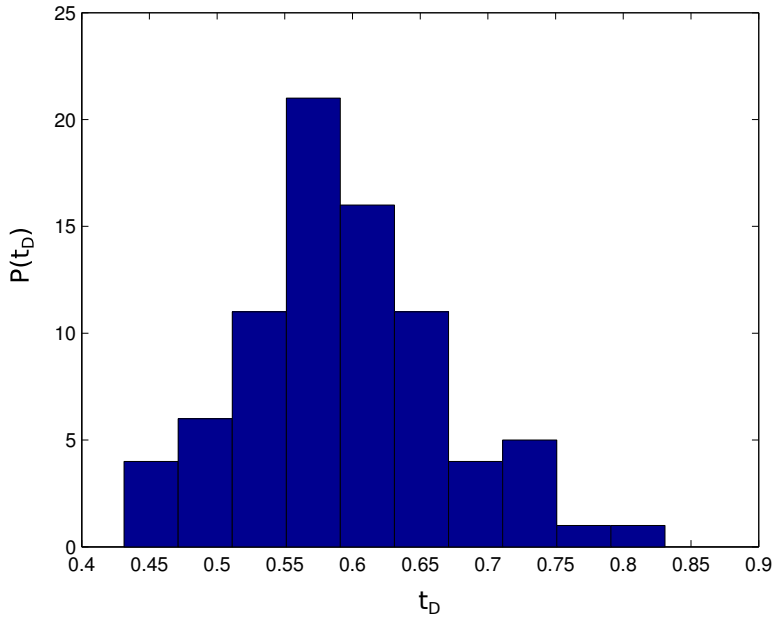

Fig. 23: The distribution of translocation times t_D (scaled into the unit interval) for $N_b = 5$ and $\Delta V = 60$ mV is positively skewed.

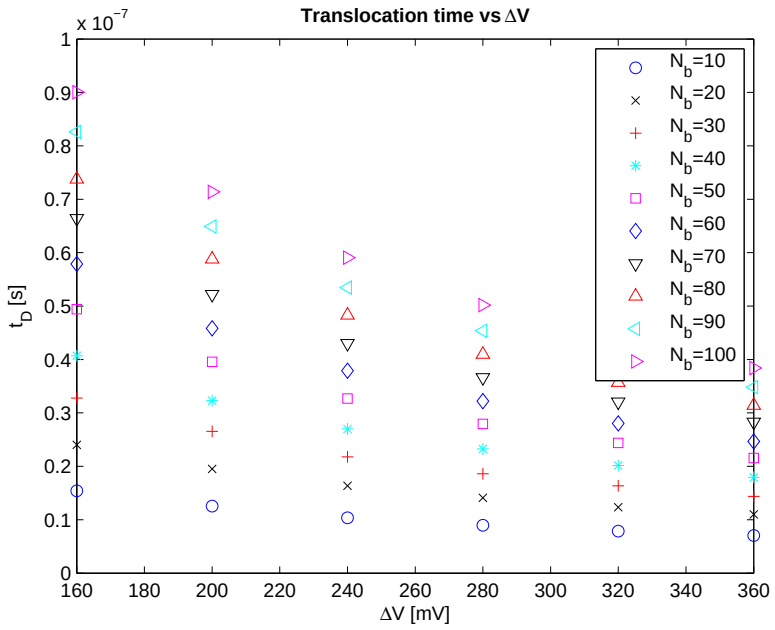

Fig. 24: Translocation time vs applied voltage (FG model)

When comparing our translocation times of the coarse-grained (Fig. 22) with the experimental values [49], we observe a difference of about 4 orders of magnitude, which corresponds to the difference in the friction coefficient used, as confirmed in Fig. 25: while matching the friction coefficient to the experiment yields $\zeta = 1\times10^{-8}$ kg/s, the one used in the simulation (based on the Stokes-Einstein relation) yields $\zeta = 3.8\times10^{-12}$ kg/s. The reason for this discrepancy is presumably the absence of counterion-driven electroosmotic flow in our model, which increases the effective friction leading to electrophoretic retardation. Furthermore, as suggested by analytical corrections to the effective drag coefficient [74] derived in the context of hindered diffusion, we also expect a contribution to the friction coefficient arising from wall-mediated hydrodynamic interactions. While the velocity disturbance generated by the counter-ion charge density can be included in the Navier-Stokes equation 16, we account for both effects in our Brownian dynamics model in [29].

For comparison and scaling, we also performed electrophoretic simulations in free solution with the fine-grained model. The translocation time t_D was now based on the movement of the center-of-mass and the electric field was active everywhere in the domain. The initial conformation of the chain is unbounded self-avoiding random walk and no equilibration is performed. Fig. 26 shows the dependence of the translocation time in pore and in free solution on chain length for a range of Peclet numbers. We observe that the velocity (and, by extension, electrophoretic mobility) is independent of chain length in the bulk solution as consistent with Rouse dynamics for high salt concentrations of the solvent. In the pore, however, the translocation time undergoes the transition from the supralinear to linear regime and continues to increase with chain length, which can be explained by the monotonically increasing bead-wall collision frequency for longer chains.

Fig. 27-28 show the chain length dependence of the electrophoretic mobility in pore and free solution. While mobility decrease with increasing chain length is consistent with similar findings of free-draining molecular dynamics simulations of short chains [23], it contradicts experimental results, which confirms non-negligible influence of hydrodynamic interactions.

To explore the effects of hydrodynamic interactions on the electrophoretic mobility, we applied the coarse-grained hybrid model to short chains, with $N_b = 1 \ldots 5$. By measuring the Stokeslet velocity field generated in response to a point force, we determined the friction renormalization correction, $\zeta_{corr} \equiv \zeta_{eff}/\zeta_{Stokes-Einstein}$, to be 0.59. The scaled electrophoretic mobility in the pore again confirmed independence on Pe, but now also showed almost no dependence on the number of beads N_b for all voltages in the range between 160 and 360 mV, with $\mu_{pore}/\mu_0 \approx 0.05$. Such behavior is indeed closer to the observed experimental dependence, which saturates at a constant value after a few base pairs [23].

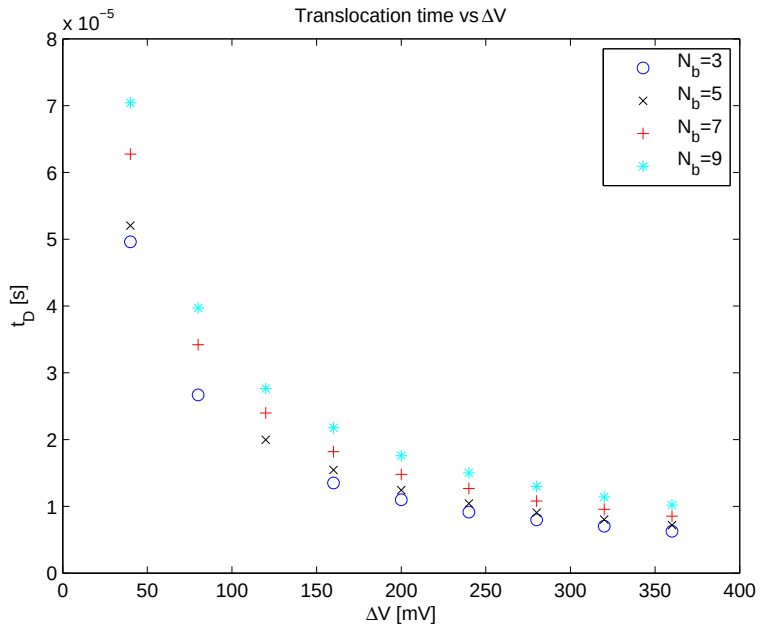

Fig. 25: Translocation time vs applied voltage (CG model) with a fitted friction coefficient $\zeta = 1 \times 10^{-8}$ kg/s. Experimental values recovered.

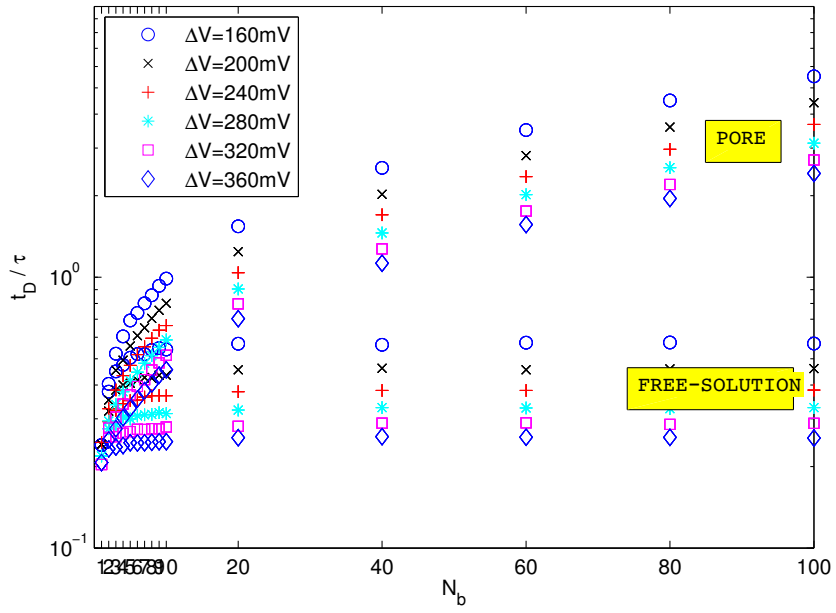

Fig. 26: Translocation time (scaled by $\tau = \zeta q_0^2/k_bT = 1.47 \times 10^{-8}$ s) in pore and free solution versus number of monomers. Fine-grained model.

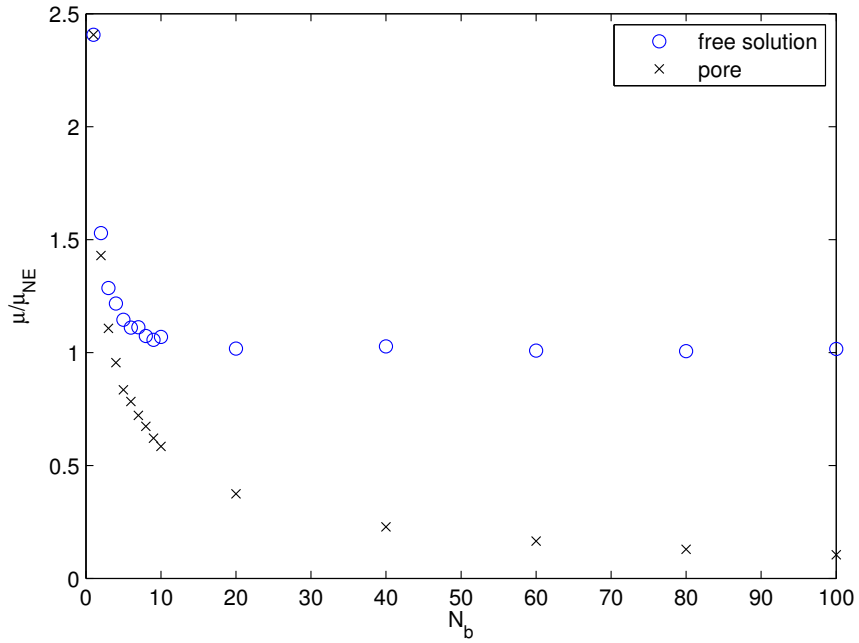

Fig. 27: Electrophoretic mobility (scaled by the Nernst-Einstein mobility $\mu_{NE} = Q/6\pi\eta a$) in pore and free-solution versus number of monomers at $Pe = 2$ ($\Delta V = 160$ mV). Fine-grained model.

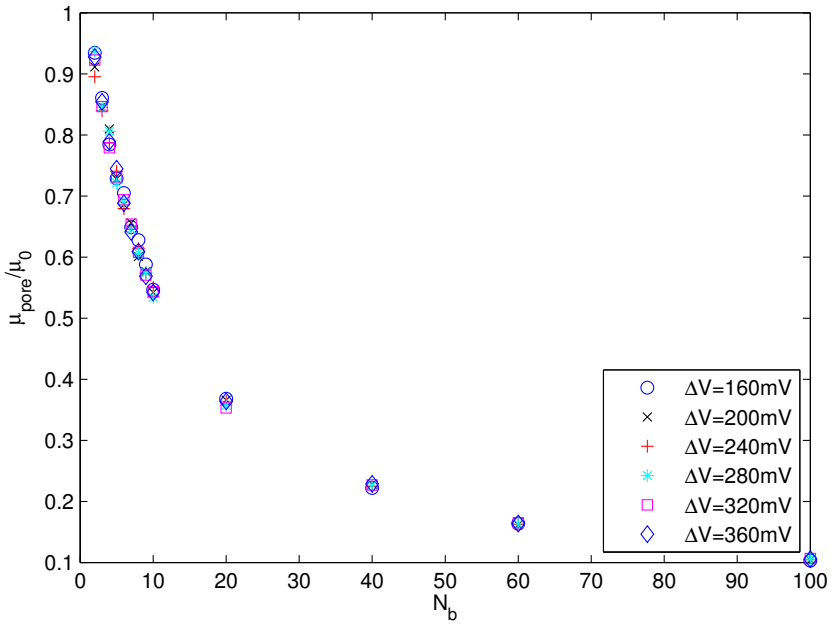

Fig. 28: Electrophoretic mobility (scaled by the free-solution electrophoretic mobility μ_0) in pore versus number of monomers. Fine-grained model.

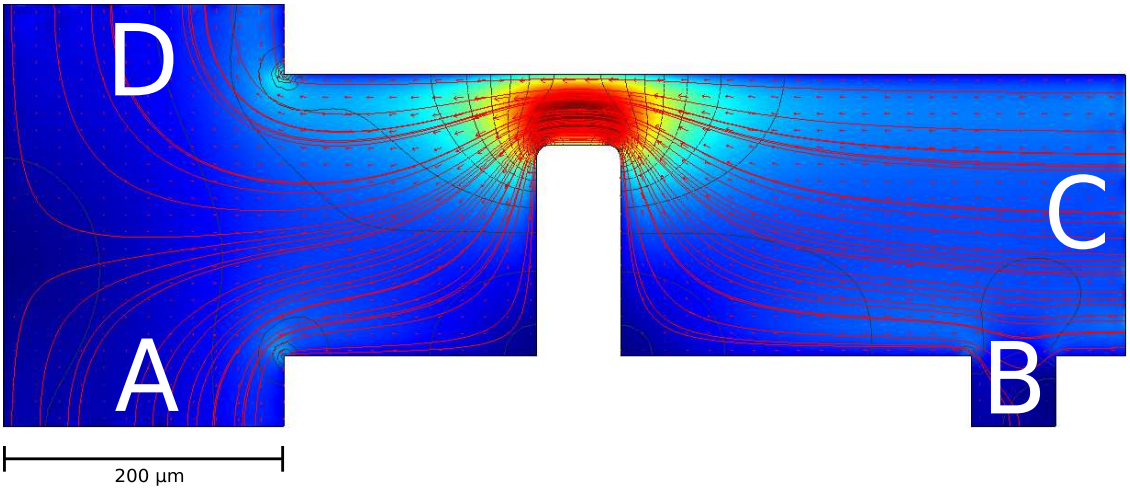

Fig. 29: Kang's DEP separator, 2D projection. Obstacle in the middle; ports A and D are outlets for separated particles, port B delivers a mixture of variable-sized particles, port C introduces buffer solution. Streamlines and contours of the electroosmotic velocity field denoted in red and black, respectively. Magnitude of the field color-coded with warmer colors corresponding to higher velocities. Due to the similitude between velocity and electric field, the same picture is also qualitatively correct for the electric field strength.

A iDEP-based particle separation

Kang's device [36] features an insulating obstacle of a rectangular cross-section, not unlike those used in entropic traps (Fig. 29). Aside from the drag force, particles experience electrophoretic (EP) and dielectrophoretic forces, governed by Eq. (5) and (6), respectively. The underlying electroosmotic (EO) flow, $\mathbf{u}_{EO}$, can be determined by three different approaches, listed in the order of increasing complexity: (i) similitude between $\mathbf{u}_{EO}$ and E, i.e. $\mathbf{u} = \mu E$ with μ being the characteristic mobility; (ii) steady-steady Navier-Stokes equation subject to the Helmholtz-Smoluchowski slip boundary condition of the form of (i); (iii) same as (ii), with the slip boundary condition replaced by no-slip and an additional electric body force term appearing in the governing equation, $\mathbf{f}_{EL} = \rho_f \mathbf{E}$, where ρ_f is the volumetric free-charge density. The equivalence of (ii) and (iii) in the limit of a thin EDL can be shown by van Dyke's asymptotic matching of the inner solution in EDL to the outer solution in the bulk electrolyte. Since (ii) effectively replaces EDL with a slip boundary, it assumes a thin EDL, $\kappa a \gg 1$, while (iii) additionally assumes uniform wall potential, insulating walls and low Re and $ReSr$ [59], where Sr is the Strouhal number. Note that while vorticity is generated at the walls (and particle locations, if HIs are taken into account), the curl of the electric body force confines it only to EDL; vorticity in the bulk is thus canceled, as consistent with the Helmholtz-Smoluchowski plug flow. The cubic dependence of particle size on the magnitude of negative DEP force, Eq. (6), indicates that larger particles will experience stronger repulsion from electric field maxima near the leading corner of the obstacle. This induces cross-wise migration to the neighboring streamlines with an increased likelihood of terminating in the upper outlet. Shape and dimensions of the geometry, as well as the applied voltages, allow one to tune the separation properties of the device as needed.

A heuristic correction factor c, determined by matching simulation results to the experiment, has been suggested [36] and used [75] to account for finite size of particles and possibly other effects. While the authors simulated tracers in 2D, we found that c, which pre-multiplies the right-hand side of Eq. (6), is sensitive to the neglect of particle inertia and dimensionality reduction; while treating particles as tracers required using $3c$ to achieve the same separation as for the inertial particles, reduction from 3D to 2D required the use of $2c$. The results for the dimensionality reduction will, however, depend strongly on edge effects and therefore on the aspect ratio. Since [36] does not discuss dimensions of the device, we used a length to width ratio of 8; the overlapping grid used for the computation is depicted in Fig. 30.

Motivated by the effort to minimize the number of adjustable parameters, we instead attempt to quantify these effects more precisely, starting with a DEP force formula more general than Eq. (6), based on multipole expansion. Note that equivalent expression can be obtained by integrating the Maxwell electric stress tensor,

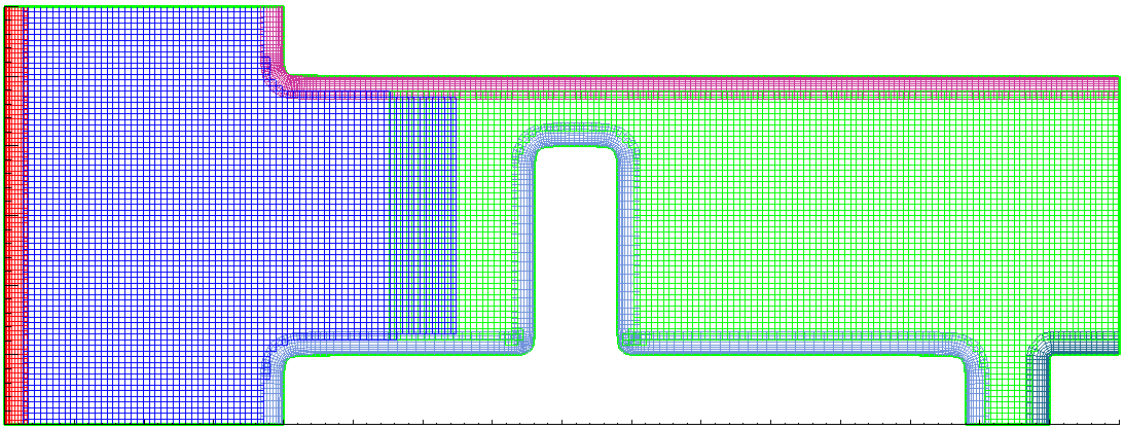

Fig. 30: Kang's DEP separator, 2D projection, overlapping grid used for the finite-difference discretization.

$\mathbf{T}^e = -1/2\epsilon_f E^2\mathbf{n} + \epsilon_f \mathbf{E}\,(\mathbf{E}\cdot\mathbf{n})$ over the surface of the particle. The $n-$th multipolar contribution can be expressed as [35]

$$\mathbf{F}^{(n)}_{DEP} = \frac{4\pi\epsilon_f a^{2n+1}}{(n-1)!\,(2n-1)!!} K^{(n)}_{CM} (\nabla)^{n-1}\mathbf{E}[\cdot]^n (\nabla)^n \mathbf{E}, \tag{55}$$

where $(2n-1)!! \equiv (2n-1)\cdot(2n-3)\cdot\ldots\cdot 5\cdot 3\cdot 1$ and $[\cdot]^n$ means n dyadic multiplications. Using Einstein summation convention (all repeated indices are summed), the first two terms of the i-th component of the force, dipole and quadrupole, are then

$$(F_{DEP})_i = 4\pi\epsilon_f a^3 \left\{ -\frac{1}{2} E_m \frac{\partial E_i}{\partial x_m} - \frac{1}{9} a^2 E_m \frac{\partial E_n}{\partial x_m}\frac{\partial^2 E_i}{\partial x_n \partial x_m} - \ldots \right\}. \tag{56}$$

Note that the dipole can be written in the more familiar form as the product of the effective induced dipole moment $\mathbf{p}_{eff} = 4\pi\epsilon_f a^3 K_{CM}\mathbf{E}$ and the gradient of the electric field,

$$\mathbf{F}^{(1)}_{DEP} = (\mathbf{p}_{eff}\cdot\nabla)\,\mathbf{E} = 2\pi\epsilon_f a^3 K_{CM}\cdot\nabla|\mathbf{E}|^2. \tag{57}$$

For the geometry depicted in Fig. 29, with voltages A = 20, B = 850, C = 900 and D = 0 V, $\kappa = 10^5$ m^{-1} and $a = 15$ μm, we found the quadrupolar correction, defined as the ratio of the magnitudes of the consecutive multipoles, $c_Q \equiv F^{(2)}/F^{(1)}$, to be about 10%. Since [36] reported c of 60-70%, more research is needed to identify other possible contributions. Obviously, the correction depends on the particle radius a (quadratically), as well as electric field non-uniformities, external voltages and geometry.

References

[1] P. Ahlrichs and B. Dünweg, *Lattice-Boltzmann simulation of polymer-solvent systems*, International Journal of Modern Physics C **9** (1998), no. 08, 1429–1438.

[2] _____, *Simulation of a single polymer chain in solution by combining lattice Boltzmann and molecular dynamics*, arXiv preprint cond-mat/9905183 (1999).

[3] A. Aksimentiev, J.B. Heng, G. Timp, and K. Schulten, *Microscopic kinetics of DNA translocation through synthetic nanopores*, Biophysical journal **87** (2004), no. 3, 2086–2097.

[4] BJ Alder and TE Wainwright, *Decay of the velocity autocorrelation function*, Physical review A **1** (1970), no. 1, 18.

[5] S. Arya, D.M. Mount, N.S. Netanyahu, R. Silverman, and A.Y. Wu, *An optimal algorithm for approximate nearest neighbor searching fixed dimensions*, Journal of the ACM (JACM) **45** (1998), no. 6, 891–923.

[6] C.L. Asbury, A.H. Diercks, G. van den Engh, et al., *Trapping of DNA by dielectrophoresis*, Electrophoresis **23** (2002), no. 16, 2658–2666.

[7] P.J. Atzberger, P.R. Kramer, and C.S. Peskin, *A stochastic immersed boundary method for fluid-structure dynamics at microscopic length scales*, Journal of Computational Physics **224** (2007), no. 2, 1255–1292.

[8] J.B. Bell, A.L. Garcia, and S.A. Williams, *Numerical methods for the stochastic Landau-Lifshitz Navier-Stokes equations*, Physical Review E **76** (2007), no. 1, 016708.

[9] H.J.C. Berendsen, *Simulating the physical world: hierarchical modeling from quantum mechanics to fluid dynamics*, Cambridge University Press, 2007.

[10] O. Berk Usta, A.J.C. Ladd, and J.E. Butler, *Lattice-Boltzmann simulations of the dynamics of polymer solutions in periodic and confined geometries*, The Journal of chemical physics **122** (2005), no. 9, 094902–094902.

[11] JR Blake, *A note on the image system for a Stokeslet in a no-slip boundary*, Proc. Camb. Phil. Soc, vol. 70, Cambridge Univ Press, 1971, pp. 303–310.

[12] ZI Botev, *Nonparametric density estimation via diffusion mixing*, The University of Queensland, Postgraduate Series (2007).

[13] AT Chan and AT Chwang, *The unsteady stokeslet and oseenlet*, Proceedings of the Institution of Mechanical Engineers, Part C: Journal of Mechanical Engineering Science **214** (2000), no. 1, 175–179.

[14] B. Cichocki and BU Felderhof, *Velocity autocorrelation function of interacting Brownian particles*, Physical Review E **51** (1995), no. 6, 5549.

[15] R. Cortez, *The method of regularized Stokeslets*, SIAM Journal on Scientific Computing **23** (2001), no. 4, 1204–1225.

[16] T. Das, S. Das, and S. Chakraborty, *Influences of streaming potential on cross stream migration of flexible polymer molecules in nanochannel flows*, The Journal of chemical physics **130** (2009), 244904.

[17] D.L. Ermak and JA McCammon, *Brownian dynamics with hydrodynamic interactions*, The Journal of chemical physics **69** (1978), 1352.

[18] E. Fares and W. Schröder, *A differential equation for approximate wall distance*, International journal for numerical methods in fluids **39** (2002), no. 8, 743–762.

[19] C. Forrey and M. Muthukumar, *Langevin dynamics simulations of ds-DNA translocation through synthetic nanopores*, The Journal of chemical physics **127** (2007), 015102.

[20] S. Frank and R.G. Winkler, *Mesoscale hydrodynamic simulation of short polyelectrolytes in electric fields*, The Journal of chemical physics **131** (2009), 234905.

[21] D. Frenkel and B. Smit, *Understanding molecular simulation: from algorithms to applications*, vol. 1, Academic press, 2001.

[22] M.D. Graham, *Fluid dynamics of dissolved polymer molecules in confined geometries*, Annual Review of Fluid Mechanics **43** (2011), 273–298.

[23] K. Grass, U. Böhme, U. Scheler, H. Cottet, and C. Holm, *Importance of hydrodynamic shielding for the dynamic behavior of short polyelectrolyte chains*, Physical review letters **100** (2008), no. 9, 96104.

[24] K. Grass and C. Holm, *Mesoscale modelling of polyelectrolyte electrophoresis*, Faraday discussions **144** (2010), 57–70.

[25] P.M. Gresho and R.L. Sani, *On pressure boundary conditions for the incompressible Navier-Stokes equations*, International Journal for Numerical Methods in Fluids **7** (1987), no. 10, 1111–1145.

[26] J. Han and H.G. Craighead, *Characterization and optimization of an entropic trap for DNA separation*, Analytical chemistry **74** (2002), no. 2, 394–401.

[27] J. Han, SW Turner, and HG Craighead, *Entropic trapping and escape of long DNA molecules at submicron size constriction*, Physical review letters **83** (1999), no. 8, 1688–1691.

[28] W.D. Henshaw and N.A. Petersson, *A split-step scheme for the incompressible Navier-Stokes equations*, Numerical simulations of incompressible flows (Half Moon Bay, CA, 2001) (2003), 108–125.

[29] P. Hotmar and R. Chella, *Brownian dynamics of polymer migration in combined pressure-driven and electrophoretic flows*, pre-print.

[30] ———, *Kinetic theory of a charged FENE dumbell in confined flow under applied pressure and electric fields*, pre-print.

[31] X. Hu, *Simulations of single molecular dynamics in hydrodynamic and electrokinetic flows*, Ph.D. thesis, The Ohio State University, 2006.

[32] I. Huopaniemi, K. Luo, T. Ala-Nissila, and S.C. Ying, *Langevin dynamics simulations of polymer translocation through nanopores*, arXiv preprint cond-mat/0608506 (2006).

[33] R.M. Jendrejack, D.C. Schwartz, J.J. De Pablo, and M.D. Graham, *Shear-induced migration in flowing polymer solutions: Simulation of long-chain DNA in microchannels*, The Journal of chemical physics **120** (2004), 2513.

[34] R.M. Jendrejack, D.C. Schwartz, M.D. Graham, and J.J. De Pablo, *Effect of confinement on DNA dynamics in microfluidic devices*, The Journal of chemical physics **119** (2003), 1165.

[35] T.B. Jones, *Basic theory of dielectrophoresis and electrorotation*, Engineering in Medicine and Biology Magazine, IEEE **22** (2003), no. 6, 33–42.

[36] K.H. Kang, Y. Kang, X. Xuan, and D. Li, *Continuous separation of microparticles by size with Direct current-dielectrophoresis*, Electrophoresis **27** (2005), no. 3, 694–702.

[37] J.J. Kasianowicz, E. Brandin, D. Branton, and D.W. Deamer, *Characterization of individual polynucleotide molecules using a membrane channel*, Proceedings of the National Academy of Sciences **93** (1996), no. 24, 13770–13773.

[38] J.M. Kim and P.S. Doyle, *A Brownian dynamics-finite element method for simulating DNA electrophoresis in nonhomogeneous electric fields*, The Journal of chemical physics **125** (2006), 074906.

[39] P.R. Kramer, C.S. Peskin, and P.J. Atzberger, *On the foundations of the stochastic immersed boundary method*, Computer Methods in Applied Mechanics and Engineering **197** (2008), no. 25, 2232–2249.

[40] R.G. Larson, *The rheology of dilute solutions of flexible polymers: Progress and problems*, Journal of rheology **49** (2005), 1.

[41] S. Lomholt, *Numerical investigations of macroscopic particle dynamics in microflows*, Ph.D. thesis, PhD thesis, Technical University of Denmark, 2001.

[42] C. Lowe and M. Dreischor, *Simulating the dynamics of mesoscopic systems*, Novel Methods in Soft Matter Simulations (2004), 2272–2272.

[43] D.K. Lubensky and D.R. Nelson, *Driven polymer translocation through a narrow pore*, Biophysical journal **77** (1999), no. 4, 1824–1838.

[44] K. Luo, T. Ala-Nissila, and S.C. Ying, *Polymer translocation through a nanopore: A two-dimensional Monte Carlo study*, The Journal of chemical physics **124** (2006), 034714.

[45] H. Ma, *Dynamics of flowing polymer solutions under confinement*, Ph.D. thesis, UNIVERSITY OF WISCONSIN, 2007.

[46] RS Marinova, CI Christov, and TT Marinov, *A fully coupled solver for incompressible Navier–Stokes equations using operator splitting*, International Journal of Computational Fluid Dynamics **17** (2003), no. 5, 371–385.

[47] S. Matysiak, A. Montesi, M. Pasquali, A.B. Kolomeisky, and C. Clementi, *Dynamics of polymer translocation through nanopores: Theory meets experiment*, Physical review letters **96** (2006), no. 11, 118103.

[48] J.A. McLennan, *Introduction to nonequilibrium statistical mechanics*, Prentice Hall Englewood Cliffs, 1989.

[49] A. Meller, L. Nivon, and D. Branton, *Voltage-driven DNA translocations through a nanopore*, Physical Review Letters **86** (2001), no. 15, 3435–3438.

[50] R. Mittal and G. Iaccarino, *Immersed boundary methods*, Annu. Rev. Fluid Mech. **37** (2005), 239–261.

[51] M. Muthukumar, *Mechanism of DNA transport through pores*, Annu. Rev. Biophys. Biomol. Struct. **36** (2007), 435–450.

[52] ———, *Polymer translocation*, CRC, 2009.

[53] H.C. Öttinger, *Velocity field in nondraining polymer chains*, Rheologica acta **35** (1996), no. 2, 134–138.

[54] H.C. Öttinger and Y. Rabin, *Diffusion equation versus coupled Langevin equations approach to hydrodynamics of dilute polymer solutions*, Journal of rheology **33** (1989), no. 5, 725–743.

[55] A.S. Panwar and S. Kumar, *Time scales in polymer electrophoresis through narrow constrictions: a Brownian dynamics study*, Macromolecules **39** (2006), no. 3, 1279–1289.

[56] N.A. Petersson, *Stability of pressure boundary conditions for Stokes and Navier–Stokes equations*, Journal of Computational Physics **172** (2001), no. 1, 40–70.

[57] C. Pozrikidis, *Boundary integral and singularity methods for linearized viscous flow*, no. 8, Cambridge University Press, 1992.

[58] M. Rubinstein and R. Colby, *Polymer Physics (Chemistry)*, Oxford University Press, USA, 2003.

[59] JG Santiago, *Electroosmotic flows in microchannels with finite inertial and pressure forces*, Analytical Chemistry **73** (2001), no. 10, 2353–2365.

[60] C.M. Schroeder, E.S.G. Shaqfeh, and S. Chu, *Effect of hydrodynamic interactions on DNA dynamics in extensional flow: Simulation and single molecule experiment*, Macromolecules **37** (2004), no. 24, 9242–9256.

[61] M. Serrano and P. Espanol, *Thermodynamically consistent mesoscopic fluid particle model*, Physical Review E **64** (2001), no. 4, 046115.

[62] J.A. Sethian, *Level set methods and fast marching methods: evolving interfaces in computational geometry, fluid mechanics, computer vision, and materials science*, vol. 3, Cambridge university press, 1999.

[63] E.S.G. Shaqfeh, *The dynamics of single-molecule DNA in flow*, Journal of non-newtonian fluid mechanics **130** (2005), no. 1, 1–28.

[64] A. Sierou and J.F. Brady, *Accelerated Stokesian dynamics simulations*, Journal of Fluid Mechanics **448** (2001), no. 1, 115–146.

[65] D.E. Smith, T.T. Perkins, and S. Chu, *Dynamical scaling of DNA diffusion coefficients*, Macromolecules **29** (1996), no. 4, 1372–1373.

[66] K. Srinivas and C.A.J. Fletcher, *Computational techniques for fluid dynamics*, Springer, 1992.

[67] E. Stellwagen, Y. Lu, and N.C. Stellwagen, *Unified description of electrophoresis and diffusion for DNA and other polyions*, Biochemistry **42** (2003), no. 40, 11745–11750.

[68] M. Streek, F. Schmid, T.T. Duong, and A. Ros, *Mechanisms of DNA separation in entropic trap arrays: a Brownian dynamics simulation*, Journal of biotechnology **112** (2004), no. 1, 79–89.

[69] W. Sung and PJ Park, *Polymer Translocation through a Pore in a Membrane*, Physical review letters **77** (1996), no. 4, 783–786.

[70] P. Tian and G.D. Smith, *Translocation of a polymer chain across a nanopore: A Brownian dynamics simulation study*, The Journal of chemical physics **119** (2003), 11475.

[71] P.T. Underhill and P.S. Doyle, *On the coarse-graining of polymers into bead-spring chains*, Journal of non-newtonian fluid mechanics **122** (2004), no. 1, 3–31.

[72] S.A. Williams, J.B. Bell, and A.L. Garcia, *Algorithm refinement for fluctuating hydrodynamics*, Multiscale Modeling & Simulation **6** (2008), no. 4, 1256–1280.

[73] C.T.A. Wong and M. Muthukumar, *Scaling theory of polymer translocation into confined regions*, Biophysical journal **95** (2008), no. 8, 3619–3627.

[74] N.J. Woo, E.S.G. Shaqfeh, and B. Khomami, *Effect of confinement on dynamics and rheology of dilute DNA solutions. I. Entropic spring force under confinement and a numerical algorithm*, Journal of Rheology **48** (2004), 281.

[75] J. Zhu, T.R.J. Tzeng, G. Hu, and X. Xuan, *DC dielectrophoretic focusing of particles in a serpentine microchannel*, Microfluidics and nanofluidics **7** (2009), no. 6, 751–756.

[76] R. Zwanzig, *Nonequilibrium statistical mechanics*, Oxford University Press, USA, 2001.